

Golden gravitational lensing systems from the Sloan Lens ACS Survey. II. SDSS J1430+4105: A precise inner total mass profile from lensing alone

Thomas Eichner^{1,2*}, Stella Seitz^{1,2}, Anne Bauer^{1,3}

¹ *Universitäts-Sternwarte München, Scheinerstr. 1, 81679 Muenchen, Germany*

² *Max-Planck-Institut für extraterrestrische Physik, Giessenbachstraße, 85748 Garching, Germany*

³ *Institut de Ciències de l'Espai, CSIC/IEEC, F. de Ciències, Torre C5 par-2, Barcelona 08193, Spain*

Accepted 2012 August 28. Received 2012 August 28; in original form 2012 June 28

ABSTRACT

We study the Sloan Lens ACS survey (SLACS) strong lensing system SDSS J1430+4105 at $z_l = 0.285$. The lensed source ($z_s = 0.575$) of this system has a complex morphology with several subcomponents. Its subcomponents span a radial range from 4 kpc to 10 kpc in the plane of the lens. Therefore we can constrain the slope of the total projected mass profile around the Einstein radius from lensing alone. We measure a density profile that is slightly but not significantly shallower than isothermal at the Einstein radius. We decompose the mass of the lensing galaxy into a de Vaucouleurs component to trace the stars and an additional dark component. The spread of multiple image components over a large radial range also allows us to determine the amplitude of the de Vaucouleurs and dark matter components separately. We get a mass to light ratio of $\frac{M_{\text{deVauc}}}{L_B} \approx (5.5 \pm 1.5) \frac{M_\odot}{L_{\odot,B}}$ and a dark matter fraction within the Einstein radius of $\approx 20\%$ to 40% . Modelling the star formation history assuming composite stellar populations at solar metallicity to the galaxy's photometry yields a mass to light ratio of $\frac{M_{*,\text{salp}}}{L_B} \approx 4.0_{-1.3}^{+0.6} \frac{M_\odot}{L_{\odot,B}}$ and $\frac{M_{*,\text{chab}}}{L_B} \approx 2.3_{-0.8}^{+0.3} \frac{M_\odot}{L_{\odot,B}}$ for Salpeter and Chabrier IMFs, respectively. Hence, the mass to light ratio derived from lensing is more Salpeter-like, in agreement with results for massive Coma galaxies and other nearby massive early type galaxies. We examine the consequences of the galaxy group in which the lensing galaxy is embedded, showing that it has little influence on the mass to light ratio obtained for the de Vaucouleurs component of the lensing galaxy. Finally, we decompose the projected, azimuthally averaged 2D density distribution of the de Vaucouleurs and dark matter component of the lensing signal into spherically averaged 3D density profiles. We can show that the 3D dark and luminous matter density within the Einstein radius ($R_{\text{Ein}} \approx 0.6R_{\text{eff}}$) of this SLACS galaxy is similar to the values of Coma galaxies with the same velocity dispersions.

Key words: gravitational lensing: strong – galaxies: elliptical and lenticular, cD – galaxies: haloes – galaxies: individual: SDSSJ 1430+4105

1 INTRODUCTION

Early-type galaxies contain a large fraction of the total stellar mass observed in the Universe (e.g., Fukugita et al. 1998; Bell et al. 2003). Studying the internal structure of early-type galaxies is crucial for understanding the baryonic physics that plays a key role in the formation and evolution of these objects. Several studies have shown that the stars

assembled in early-type galaxies are embedded in massive dark matter haloes (e.g., Gavazzi et al. 2008; Lagatutta et al. 2010; Weijmans et al. 2008), but the precise amount of dark matter contained in the galaxies' inner regions is still under debate.

Dark matter only simulations have found indications of a universal density profile for dark matter haloes, present also in galaxies (the so called NFW profile; Navarro et al. 1996). Nevertheless, more recent and realistic simulations that include also the physics of baryons (e.g., Gnedin et al.

* E-mail: eichner@usm.lmu.de

2004; Duffy et al. 2010; El-Zant et al. 2001; Bertin et al. 2003; Ma & Boylan-Kolchin 2004; Blumenthal et al. 1986; Jesseit et al. 2002), like radiative cooling and supernova and black hole feedback, have suggested that the inner profile of the dark matter component can be significantly affected by the interactions between baryonic and dark matter.

The internal structure of nearby early-type galaxies has been for decades the object of intense dynamical analyses (e.g., Saglia et al. 1992; Gerhard et al. 2001; Thomas et al. 2007; Thomas et al. 2009; Thomas et al. 2011; Pu et al. 2010). One focus of these studies is to compare stellar with dynamical mass to light ratios. The dynamical studies, e.g. Gerhard et al. (2001), Thomas et al. (2011) find ratios for nearby elliptical galaxies of $M/L_B \approx 4$ to 10. Similar values are also found by Cappellari et al. (2006). Only in the last few years has gravitational lensing also contributed significantly to our understanding of the luminous and dark matter composition of early-type galaxies beyond the local Universe (Barnabè et al. 2009; Grillo et al. 2010; Barnabè et al. 2010). Strong gravitational lensing in early-type galaxies has also proved to be a powerful cosmological tool to probe the geometry of the universe independently from other diagnostics (e.g., Grillo et al. 2008a; Suyu et al. 2009, 2010).

By combining strong gravitational lensing and stellar dynamics in a sample of first 15, then 58 early-type galaxies, Koopmans et al. (2006) and Koopmans et al. (2009) have found that the average total (luminous and dark) mass density distribution within the effective radius – the radius of the isophote containing half of the total light of the galaxy – is well represented by an isothermal distribution ($\rho \propto r^{-2}$), although significant deviations from this result can be observed in individual galaxies. Only rare systems where an extended or several distinct sources are gravitationally lensed over an extended radial area on the lens plane can be used to determine the total mass density profile of the lens galaxy over a wide radial range through lensing only (e.g. Grillo et al. 2008b, 2010; Fadely et al. 2010). Moreover, combining lensing total mass measurements with photometric stellar mass estimates in these systems offers a unique way to disentangle their luminous and dark matter components.

In this paper, we study the gravitational lensing system SDSS J1430+4105 that is composed of a massive early-type galaxy acting as a lens for an irregular background source. This galaxy was part of the SLACS survey¹ and has been studied as part of their lens sample, especially in Bolton et al. (2008), Auger et al. (2009) and Auger et al. (2010): Bolton et al. (2008) fit a singular isothermal lens model to the observed multiple images, while Auger et al. (2009) and Auger et al. (2010) combine the measured Einstein radii and masses with photometric and dynamical data. The surface brightness distribution of the lensed source shows several peaks that extend from 4 to 10 kpc from the lens galaxy centre. This fact provides the opportunity to investigate the lens galaxy mass distribution on radial ranges larger than those explored in similar analyses of other gravitational lensing systems (e.g., Xanthopoulos et

al. 1998, Cohn et al. 2001, Grillo et al. 2010).

The paper is organised as follows: Section 2 gives an overview of the observations and data used in this work and introduces the environment of SDSSJ 1430+4105; Section 3 describes the details of the strong lensing models. Section 4 states the implications for the total mass and the mass profile. In Section 5 the mass to light ratio for the de Vaucouleurs component is constrained, in Section 6 the results are discussed. Appendix A contains further variants of strong lensing models. Appendix B gives further details of the environment implementation.

The cosmological model adopted in this paper is parametrized by $\Omega_m = 0.3, \Omega_\Lambda = 0.7, H_0 = 70 \text{ km s}^{-1} \text{ Mpc}^{-1}$. In the cosmology assumed, 1 arcsec in the lens ($z_l = 0.285$) and source ($z_s = 0.575$) plane corresponds to 4.30 and 6.55 kpc.

2 OBSERVATIONS

The SLACS Survey² aimed at finding strong gravitational lenses among the galaxies observed in the SDSS. The lens detection strategy is presented in Bolton et al. (2004) and is based on the examination of the SDSS galaxy spectra, taken with a 3" diameter fibre, to identify emission lines not associated with the primary target galaxy but with an additional source, aligned with the first galaxy and located at a higher redshift. The lens candidates are then ranked in terms of their probability of being lensing systems and are consequently observed with the HST/ACS and WFPC2.

Up to now, 85 confirmed (grade-A) lenses (Bolton et al. 2006, Auger et al. 2009) were discovered in this way, and SDSSJ 1430+4105 is one of these. In Fig. 1 we show the SDSS spectrum, from which lens and source redshifts of $z_l = 0.285$ and $z_s = 0.575$ are measured, together with the lens aperture velocity dispersion of $\sigma_{\text{SDSS}} = (322 \pm 32) \text{ km s}^{-1}$.

2.1 Galaxy light profile and lensing observables

The basic photometric and spectroscopic properties of SDSSJ 1430+4105, taken from Bolton et al. (2008), are stated in Table 1. For these, Bolton et al. (2008) fitted a de Vaucouleurs (de Vaucouleurs 1948) profile with elliptical isophotes to the galaxy's surface brightness distribution. They obtained an effective radius of $\theta_{\text{eff}} = 2.55'' = 10.96 \text{ kpc}$, a minor to major axis ratio of $q_L = 0.79$, and a major axis angle of $\Theta_{q,L} = -12.8^\circ$. The angles are transformed to the adopted local reference frame shown in Fig. 2, and measured counterclockwise with the y-axis equals to 0° .

We retrieve the public HST images from the Hubble Space Telescope archive at ESO³. Three filters were available for this system: HST/WFPC2 F606W with a total integration time of 4400s (ua114501m, ua114502m, ua114503m, ua114504m), HST/ACS F814W with a total integration time of 2128s (j9op36010) and HST/WFC3 F160W with a total integration time of 2497s. For the lensing analysis we use

¹ <http://www.slacs.org>

² <http://www.slacs.org>

³ <http://archive.eso.org/archive/hst/>

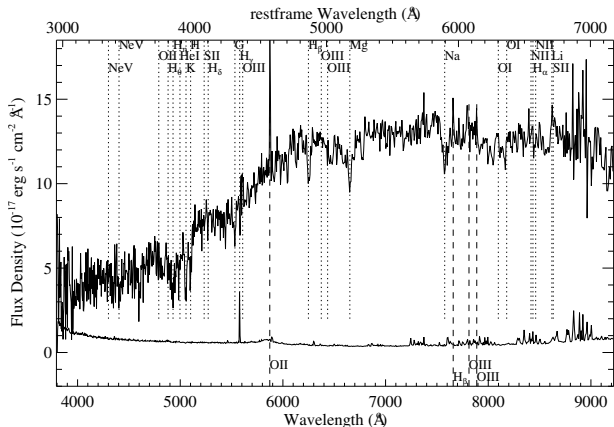


Figure 1. The SDSSJ 1430+4105 spectrum as observed by the SDSS 3'' diameter fibre. On the bottom, the observed wavelength is stated, while on the top, this is converted into the restframe wavelength of the lens ($z = 0.285$). The dotted vertical lines give the SDSS emission / absorption line sample at the redshift of the lens. The dashed vertical lines give some prominent emission lines at the redshift of the source. Overplotted in the lower part of the figure is the flux uncertainty given again by SDSS. The spectrum shows several absorption lines typical of an early type galaxy at $z = 0.285$ and some additional emission lines at redshift $z = 0.575$ (e.g. the lines at 5872\AA , 7661\AA and 7813\AA , which can be identified as the redshifted [OII]3728, $H\beta$ and [OIII]4960 lines respectively). Data taken from the Sloan digital sky survey, www.sdss.org.

the ACS F814W filter observations, since the PSF of the ACS camera is smaller than the one of the WFPC2 and WFC3. First, we subtract the lensing galaxy's light contribution with GALFIT (Peng et al. 2002) by using a de Vaucouleurs profile, with the parameters of Table 1. Then, in order to refine the lens galaxy subtraction and especially remove the residuals still present in the central region, an additional Sersic profile (Sersic 1963) with index 1.2 is subsequently subtracted.

Fig. 2 shows the final galaxy subtracted image. The lensed source has a complex surface brightness distribution, with 5 surface brightness maxima which are imaged 2 times each. We mark and label the 5×2 multiple image positions, identified as the brightest pixels, in Fig. 2. Their coordinates are reported in Table 2 together with approximate error estimates. We assume in the following that all subcomponents A-E are at the same redshift and not unlikely line-of-sight projections at different redshifts. The distances of the multiple images from the centre of the lens galaxy light distribution span a range from $0.93''$ to $2.32''$. In the rest of the paper, if not otherwise stated, we adopt the coordinate system introduced in Fig. 2 which is rotated relative to the WCS J2000 (world coordinate system) by 47.21° .

2.2 Observed environment

SDSSJ 1430+4105 is not an isolated galaxy. It coincides in redshift and location with a galaxy group at $z = 0.287$, listed in the maxBCG cluster catalogue, (Koester et al. 2007). Therefore, we should consider the light deflection by the lens' environment when we model this lens. We show the environment of SDSSJ 1430+4105 (labelled as A) in Fig. 3. The galaxy labelled as I (and called GI in the following)

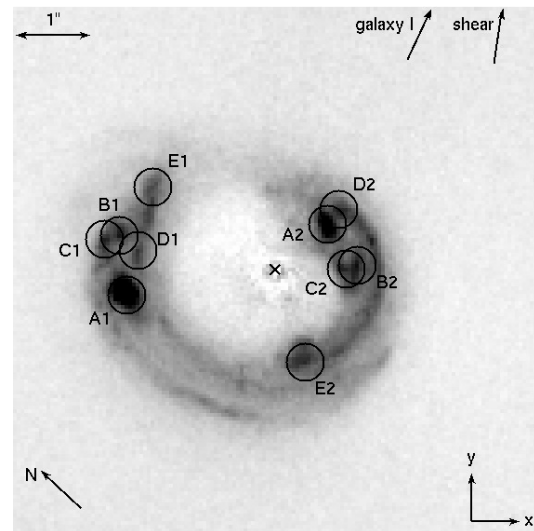


Figure 2. The multiple image systems that are identified after the lens galaxy subtraction and used as input for the lensing analysis. The labels A1 to E2 mark the positions used for the strong lensing analysis. The same letters correspond to images coming from the same source feature, the labelling is done according to Table 2. The cross marks the centre of the subtracted lens galaxy light. Also indicated are the derived shear direction from Sec. B1 and the direction of galaxy I. For orientation north is given as well. Angles are measured in the local coordinate system counterclockwise as $(-x)$ over y if not otherwise stated. The image is rotated relative to the WCS J2000 by 47.21° .

Table 2. Observed positions of the multiple image systems

ID	Θ_1^1 ('')	Θ_2^1 ('')	z_s	δ_Θ ('')	d^1 ('')
A1	-1.99	-0.32	0.575	0.05	2.02
A2	0.69	0.62	0.575	0.05	0.93
B1	-2.08	0.47	0.575	0.05	2.13
B2	1.08	0.08	0.575	0.05	1.08
C1	-2.28	0.42	0.575	0.05	2.32
C2	0.93	0.03	0.575	0.05	0.93
D1	-1.84	0.27	0.575	0.05	1.86
D2	0.84	0.80	0.575	0.05	1.35
E1	0.39	-1.21	0.575	0.05	1.27
E2	-1.64	1.11	0.575	0.05	1.98

¹relative to the centre of the galaxy light distribution

was proposed to be the brightest cluster galaxy (BCG) of this group found in Koester et al. (2007). The photometric redshift of the group GI is estimated to be $z = 0.287$ with a typical redshift error in the maxBCG catalogue of 0.01. Within this error the photometric redshift of the group is identical to the spectroscopic redshift (0.28496) of the lensing galaxy. The group consists of 12 members within the R_{200} of this group, $N_{(\text{gal}, 200)} = 12$. At this richness level, the maxBCG cluster is typically more than 90% pure and complete, based on tests with mock catalogues. We now estimate the group members based on astrometric and photometric data from SDSS DR7 (Abazajian et al. 2009). We consider each galaxy within $10'$ from the main lens J1430+4105. We allow for galaxies which have at least one of the photometric

Table 1. Photometric and spectroscopic quantities of the lens system

RA (J2000)	Dec (J2000)	z_l	z_s	q_L ($\frac{b}{a}$)	$\Theta_{q,L}$ ($^\circ$)	ϑ_{eff} ($''$)	σ_{SDSS} (km s^{-1})
14:30:04.10	+41:05:57.1	0.285	0.575	0.79	-12.8 ¹	2.55	322 ± 32

Given are the position of the galaxy (RA, Dec), the redshifts of galaxy and source (z_l z_s), the axis ratio (q_L), the orientation ($\Theta_{q,L}$), the effective radius (ϑ_{eff}) of the lens' light distribution and the velocity dispersion σ_{SDSS} .

Values are taken from Bolton et al. (2008)

¹This angle is equivalent to -59.3° in the WCS coordinate system, defined as (-E) over N.

redshift estimates (template based (Template-z) (Adelman-McCarthy et al. 2007) or neural network based (CC2 z and D1 z) (Oyaizu et al. 2008)) consistent within one standard deviation with the spectroscopic redshift value of SDSS J1430+4105 and the photometric redshift of the group GI. The neighbours which pass these requirements are listed in Table 3. This table shows that for our definition the galaxy A is a group member from both its photometric and spectroscopic redshift. The magnitudes of the galaxies A and I in the ugriz filters are 20.43, 19.02, 17.74, 17.12, 16.87 and 22.54, 19.44, 17.92, 17.35, 17.00 for A and I respectively, and thus A is formally the brightest galaxy ('BCG') of this group. Since the group membership and group redshift estimate of the maxBCG catalogue (Koester et al. 2007) is mostly based on the g-r colour, the contaminated g-r colour of A due to lensing has likely led to A not being considered as a group member and therefore as the BCG. Using the same definition for the r_{200} as stated in Koester et al. (2007) we find 11 group members from Table 3.

From Johnston et al. (2007), who tested the maxBCG cluster finder on simulated groups and clusters of galaxies, we derive the probability that a group of the richness given in the maxBCG catalogue $N_{(\text{gal},200)} = 12$ is centred on the correct BCG in the maxBCG cluster catalogue to be $p_c(N_{200} = 12) = 0.63$. Therefore both A or I could be the true mass centre of the group GI. Finally, the Koester et al. (2007) group catalogues could also contain false positive detections. Song et al. (2012) have shown that the false detection rate of such groups can be as large as 40%. This motivates why we will consider lens models with and without an external group contribution. We will show that including a galaxy group centred on galaxy I has only minor influence on the lens parameters.

3 STRONG GRAVITATIONAL LENSING

In this section we model the lens mass distribution with the public GRAVLENS (Keeton (2001a)) code (Sec. 3.1) assuming point sources and with the LENSVIEW (Wayth & Webster (2006)) code (Sec. 3.3) using the 2-dimensional surface brightness distribution of the same system. Both approaches give consistent results. We give a description of the influence of the environment on the lens model of SDSSJ 1430+4105 in Sec. 3.2.



Figure 3. The observed environment of J1430+4105, taken from SDSS. All galaxies with a photometric redshift consistent with the spectroscopic redshift of SDSSJ 1430+4105 (labelled with A and marked with a diamond) within 1 standard deviation are marked by squares. The galaxy marked as I is the BCG for the group identified by Koester et al. (2007). In the image, north is up and east is left. This image is rotated relative to Fig. 2 by 47.21° . The size is $7.5' \times 7.5'$. For the properties of the galaxies, see Table 3.

3.1 Parametric modelling using GRAVLENS

GRAVLENS⁴ is a public code that uses parametric lens models to reconstruct the properties of an observed lensing system. The lens-modelling we implement here is similar to the one of Grillo et al. (2010) where the reader can find more details. In this subsection, we use peaks in the surface brightness distribution of the lensed images as point-like position constraints for the lens model (see Table 2 and Fig. 2). Since the complex surface brightness distribution of the lensed galaxy makes it difficult to associate reliably a flux measurement to each multiple image, we neglect flux constraints. In GRAVLENS the convergence κ for a singular isothermal ellipsoid (SIE) or an ellipsoidal powerlaw (PL) is parametrized as

⁴ see <http://redfive.rutgers.edu/~keeton/gravlens>

Table 3. Observed environment of SDSSJ 1430+4105

Obj	RA (J2000)	Dec (J2000)	mag _i	σ _i	Template z	Error	NN CC2 z	Error	NN D1 z	Error	Spectro-z	Error
A	217.51704	41.0992	17.216	0.006	0.228	0.033	0.231	0.027	0.234	0.026	0.28496	2.13E-4
B	217.44551	41.0456	18.729	0.018	0.202	0.015	0.216	0.073	0.260	0.067		
C	217.45406	41.0460	18.495	0.020	0.262	0.019	0.287	0.045	0.316	0.048		
D	217.45941	41.0625	18.657	0.019	0.179	0.032	0.312	0.055	0.309	0.064		
E	217.46178	41.1010	18.870	0.016	0.266	0.019	0.287	0.055	0.343	0.073		
F	217.46445	41.0738	19.134	0.020	0.286	0.082	0.309	0.096	0.344	0.073		
G	217.47010	41.1054	18.708	0.013	0.224	0.011	0.228	0.073	0.267	0.063		
H	217.49009	41.0825	19.356	0.024	0.200	0.024	0.259	0.070	0.339	0.060		
I	217.49493	41.1044	17.348	0.008	0.273	0.019	0.272	0.020	0.272	0.016		
J	217.50190	41.0995	18.697	0.018	0.251	0.021	0.293	0.062	0.326	0.063		
K	217.50545	41.0779	18.283	0.015	0.263	0.020	0.267	0.037	0.293	0.032		
L	217.51212	41.0655	18.008	0.0100	0.268	0.015	0.273	0.022	0.279	0.023		
M	217.52402	41.1253	19.358	0.026	0.298	0.084	0.451	0.042	0.424	0.042		
N	217.54462	41.1407	18.947	0.026	0.275	0.063	0.284	0.057	0.296	0.048		
O	217.54641	41.0450	18.500	0.016	0.169	0.056	0.210	0.043	0.236	0.057		
P	217.58642	41.0746	19.373	0.027	0.371	0.088	0.401	0.059	0.403	0.064		

Properties of the galaxies considered as part of the environment of J1430+4105. Given in the rows are the object name (Obj), the position (RA, Dec), its i band magnitude mag_i and its error σ_i, and its various photometric redshift estimates together with its errors: first the template method and its error, summarised in Adelman-McCarthy et al. (2007), followed by the neural network based methods CC2 and its error and D1 and its error (Oyaizu et al. 2008).

$$\kappa(\Theta_1, \Theta_2) = \frac{b^{\beta-1}}{2(1-\epsilon)^{\frac{\beta-1}{2}} \left(\frac{\Theta_c^2}{1-\epsilon} + \Theta_1^2 + \frac{\Theta_2^2}{q^2} \right)^{\frac{\beta-1}{2}}} \quad (1)$$

with

$$\epsilon = \frac{1-q^2}{1+q^2},$$

where b is the lensing strength, β denotes the steepness of the density profile (β = 2 in the case of an isothermal profile), Θ₁ and Θ₂ are the coordinates on the plane of the sky relative to the centre of mass of the lens, Θ_c is the core radius and q is the axis ratio of the isocontours of the convergence (q = 1 for a circular mass model). In the special case of a circular lens without core radius, b equals the Einstein radius Θ_{E_{in}} of the lens defined as $\bar{\kappa}(\Theta \leq \Theta_{E_{in}}) = 1$. Further we use a de Vaucouleurs Model (de Vaucouleurs 1948) parametrized as

$$I(R) = I_e e^{-7.67 \left[\left(\frac{R}{R_{eff}} \right)^{1/4} - 1 \right]}, \quad (2)$$

with R_{eff} being the effective radius (the radius which contains half the light) and I_e the surface density at this radius. In GRAVLENS this is implemented as

$$\kappa = b_{deV} e^{-7.67 \left[\frac{(\Theta_1^2 + \Theta_2^2/q^2)^{1/2}}{\Theta_{eff}} \right]^{1/4}}. \quad (3)$$

In this parametrisation, b_{deV} is the value of the central convergence. The Einstein radius, however, depends also on Θ_{eff} and q. Also a Navarro, Frenk and White (NFW) profile (Navarro et al. 1996) is used, defined as

$$\rho(r) = \frac{\delta_c \rho_c}{r/r_s (1+r/r_s)^2}, \quad (4)$$

with ρ_c denoting the critical density of the universe at the redshift of the lens, and r_s and δ_c are characteristic properties of the individual halo. For an overview of its

lensing properties, see Wright & Brainerd (2000).

The relation for the LOS projected surface mass density Σ of the lens and lensing convergence κ is

$$\kappa = \frac{\Sigma}{\Sigma_{crit}} \quad \text{with} \quad \Sigma_{crit}^{-1} = \frac{4\pi G}{c^2} \frac{D_d D_{ds}}{D_s},$$

where D_d, D_s and D_{ds} are the angular diameter distances from the observer to the lens, the source and from the lens to the source, respectively. The goodness of a model is judged by the χ²:

$$\chi_{lens}^2 = \sum_i \frac{\| \Theta_i - \Theta_{0,i} \|^2}{\delta_{\Theta_i}^2}, \quad (5)$$

where Θ_i denote the model-predicted positions of the i-th images, Θ_{0,i} is its observed position, and δ_{Θ_i} its observed positional uncertainty.

Any priors described in the text are added to this χ² in GRAVLENS via

$$\chi_{tot}^2 = \chi_{lens}^2 + \chi_{prior}^2$$

with

$$\chi_{prior}^2 = \frac{(p - p_{prior})^2}{\sigma_{prior}^2},$$

where p is the used parameter value, p_{prior} its prior and σ_{prior} its 1σ error. Results give best-fitting parameters and their 1σ errors. The likelihood of a parameter set is given by $L \propto e^{-\chi_{tot}^2/2}$. In almost all cases, the best-fitting values are within the 68% error interval of the marginalised distributions.

The values of the parameters for the minimum χ² models are given in Tables 4 and 5. There, we give the model number, type, the best-fitting parameters of the model together with the resultant χ², the number of degrees of freedom (d.o.f.) and the reduced χ²_{red} = $\frac{\chi^2}{d.o.f.}$ of each model.

Also, the 1σ error intervals are given. These error estimates of the parameters are carried out using Monte Carlo Markov Chains (MCMC) with several thousand steps each. For each model, 10 chains are calculated with different starting points. Convergence is reached by comparing the variance of the point distribution of each of these chains with its combined distribution, see Fadely et al. (2010), Gelman et al. (1995). From the final chains, the 2nd half of each chain is combined to the final MCMC point distribution. The acceptance rate typically lies between 0.25 and 0.3. We explore potential parameter correlations from these and derive 68% confidence intervals⁵ on the parameters by exclusion of the lowest and highest 16% of the MCMC points' distribution; the central value is given by the median value of the MCMC points' distribution, since there are only small deviations between the median and the average values of the 68% and 90% error intervals.

We describe the most important different models without environment in the following: To check for the basic properties of the system, we model the lens as one component SIE (Model I) and PL (Model II) model. To derive the de Vaucouleurs masses in this lens, we combine a de Vaucouleurs component with a dark matter halo model (Model III) and show that this result is not significantly affected by also taking the environment into account (Models IV, V).

Model I : The lens is modelled as a SIE (Eq. 1 with $\beta = 2$); the environment of the lens is ignored. The free parameters of this model are the lensing strength b , the axis ratio q , and its position angle Θ_q . The best-fitting model is shown in Fig. 4. The results of the MCMC are shown in Fig. 5. The density contours describe the probability density for the parameter values, whereas the best-fitting model is marked with a cross. The reason for the apparent correlation of q and b in Fig. 5 lies in the definition of κ in Eq. 1. The marginalised 68% confidence errors are: $b = (1.49^{+0.02}_{-0.02})''$, $q = (0.71^{+0.02}_{-0.02})$ and $\Theta_q = (-21.8^{+2.5}_{-2.3})^\circ$. These values are in very good ($\approx 1\sigma$) agreement with the values derived by Bolton et al. (2008) using a similar parameterisation for the lens total mass distribution.

Model II : Model II follows a power law (PL) (Eq. 1 with arbitrary β within the limits $[1, 2.7]$), and thus has one more free parameter relative to Model I. The values for the parameter distributions are shown in Fig. 6. The marginalised distributions change to $b = (2.12^{+0.60}_{-0.32})''$, $q = (0.81^{+0.04}_{-0.07})$, $\Theta_q = (-22.2^{+2.1}_{-2.5})^\circ$ and $\beta = (1.73^{+0.21}_{-0.13})$. We observe again (see Fig. 6) that the parameters b , q and β are correlated with each other. This is entailed by the definition of the convergence κ in Eq. 1. The steepness parameter β is constrained to a value shallower than isothermal on a 1.3σ level. The orientation Θ_q stays at the same angle as in the SIE case, while its axis ratio moves towards rounder solutions, now being comparable to the axis ratio of the light distribution.

Model III : In the following, we split the mass distribution into different components. We use a de Vaucouleurs

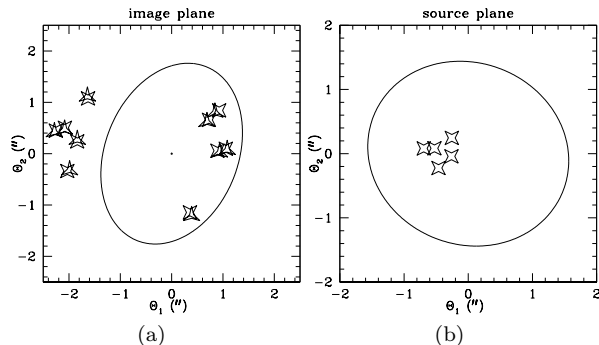


Figure 4. The best-fitting model derived with GRAVLENS for the SIE case (Model I) (see Table 4), both the image plane and the source plane are plotted. On the image plane triangles mark the input positions, while crosses mark the best-fitting model positions. On the source plane, the predicted source positions are plotted. Further, the respective critical lines (caustics) on the image (source) plane are plotted.

like component as traced by the stellar component and add dark matter with different profiles if needed. Since the de Vaucouleurs component for galaxy A alone does not provide a good model, see Appendix A, we add a dark matter component centred at galaxy A. We add an elliptical NFW-like component to the de Vaucouleurs profile. This composition resembles the common picture of galaxy mass distribution. For the dark matter halo, we impose a prior on the axis ratio based on the Bolton et al. (2008) work of $q_{\text{dark,prior}} = (0.79 \pm 0.12)$. Also we set the limit of the scale radius to values $< 500''$, approximately 10 times the value we find from Sec B2 for the scale radius. The total mass of the de Vaucouleurs component is $M_{\text{deV}} = (8.8^{+1.3}_{-1.9}) \times 10^{11} M_\odot$ while the parameters of the dark matter halo are, see Fig. 7: $q_d = (0.72^{+0.1}_{-0.1})$, $\Theta_q = (-26.0^{+2.7}_{-2.3})^\circ$, $c_d = (1.8^{+1.0}_{-0.4})$ and $r_{200} = (406^{+128}_{-129})''$. We note that there is some degeneracy between the concentration c and r_{200} . Further we have no constraints on r_{200} from the data, since we do not have observables outside $2.32''$. Using a NSIE-like dark matter component yields similar results, as described in Appendix A, Model IIIb.

3.2 Lens modelling of the environment

As mentioned before, this galaxy is not an isolated field galaxy, hence we investigate the possible impact on the derived lens parameters by taking the environment into account. In the following, we centre a smooth group contribution at galaxy I and calculate its convergence and shear at the position of SDSSJ 1430+4105. Further modelling of the group contribution by summing up the contributions of the individual members (“clumpy group”), and by centring it at galaxy A itself is discussed in Appendix B.

Smooth group mass distribution centred at galaxy I

According to Rozo et al. (2009), we can transform the group richness into a group mass of $M_{500} = (0.72 \pm 0.29) \times 10^{14} M_\odot$ within 1σ . This mass can be converted into a velocity dispersion of $\sigma_{\text{group}} = 519 \pm 107 \text{ km s}^{-1}$, using the critical density

⁵ all given errors in this section are the 68% confidence values of the marginalised distributions, unless otherwise stated

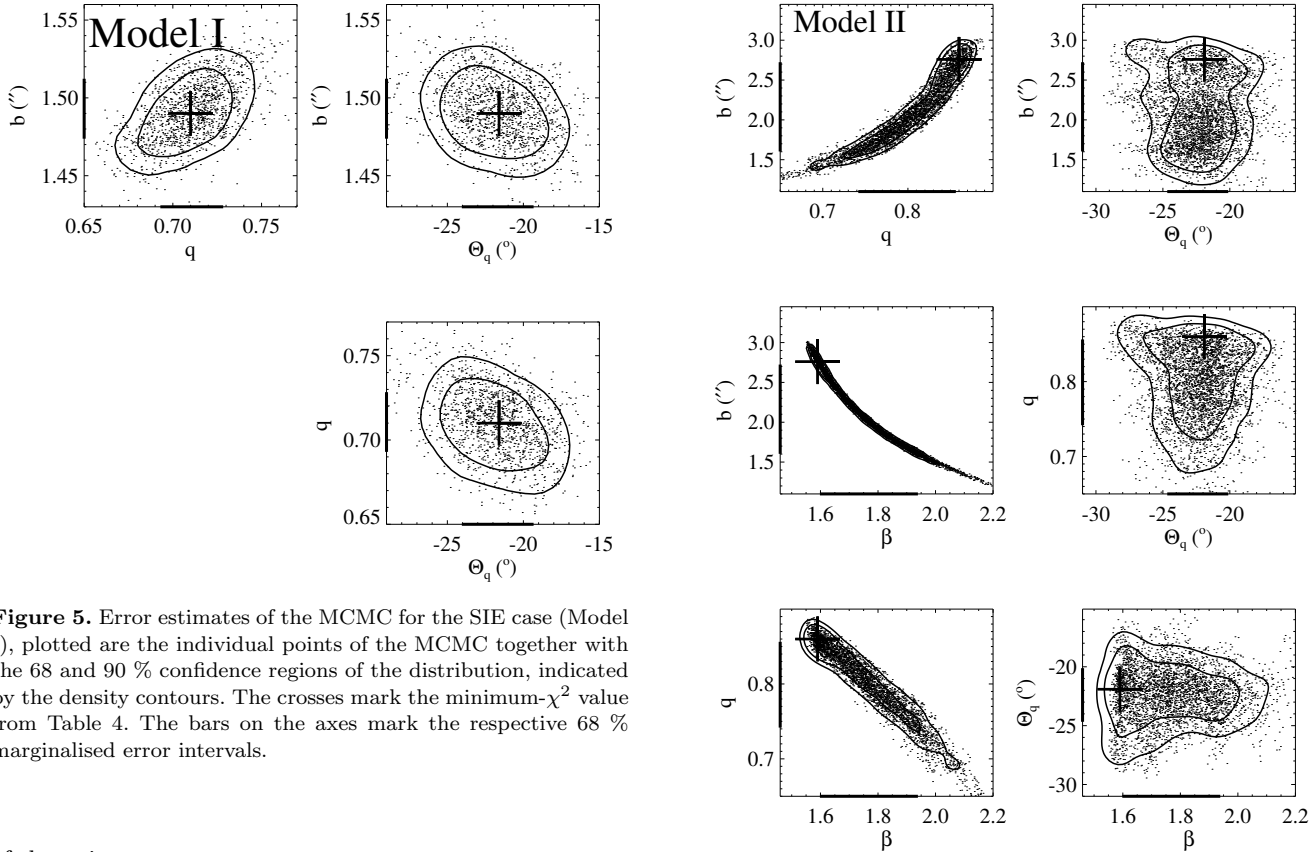
Table 4. minimum- χ^2 values and parameter estimates derived with GRAVLENS for the isothermal and powerlaw models

		b (")	q	Θ_q ($^\circ$)	β	χ^2	d.o.f.	$\frac{\chi^2}{\text{d.o.f}}$
Model I	SIE	1.49	0.71	-21.6	2.00 ¹	11.5	7	1.6
		1.47 – 1.51	0.69 – 0.73	-24.1 – -19.3				
Model II	PL	2.76	0.86	-21.9	1.59	10.1	6	1.7
		1.60 – 2.72	0.74 – 0.85	-24.7 – -20.1	1.60 – 1.94			

¹fixed value

Table 5. minimum- χ^2 values and parameter estimates derived with GRAVLENS for the two component de Vaucouleurs plus dark matter models

		M ($10^{11}M_\odot$)	q_d	$\Theta_{q,d}$ ($^\circ$)	c_d (")	r_{200}	b_{group}	χ^2	d.o.f.	$\frac{\chi^2}{\text{d.o.f}}$
Model III	deVauc+NFW	7.4	0.79	-26.1	1.7	514		7.9	5	1.6
		6.9 – 10.1	0.62 – 0.82	-28.3 – -23.3	1.4 – 2.8	277 – 534				
Model IV	deVauc+GI	13.5					8.0	18.9	8	2.4
		13.3 – 13.7					7.3 – 8.7			
Model V	deVauc+NFW+GI	9.5	0.79	-24.6	2.2	280		7.8	4	2.0
		8.7 – 11.8	0.68 – 0.90	-27.1 – -12.8	1.0 – 2.6	168 – 463	3.2 – 6.5			


Figure 5. Error estimates of the MCMC for the SIE case (Model I), plotted are the individual points of the MCMC together with the 68 and 90 % confidence regions of the distribution, indicated by the density contours. The crosses mark the minimum- χ^2 value from Table 4. The bars on the axes mark the respective 68 % marginalised error intervals.

of the universe

$$500\rho_c(z) = \frac{3M_{500}}{4\pi r_{500}^3}$$

and the singular isothermal sphere equation:

$$M_{500} = M(r_{500}) =: \frac{2\sigma_{\text{group}}^2 r_{500}}{G}.$$

Figure 6. Error estimates of the MCMC for the PL case (Model II), plotted are the individual points of the MCMC together with the 68 and 90 % confidence regions of the distribution. The crosses mark the minimum- χ^2 value from Table 4. The bars on the axes mark the respective 68 % marginalised error intervals.

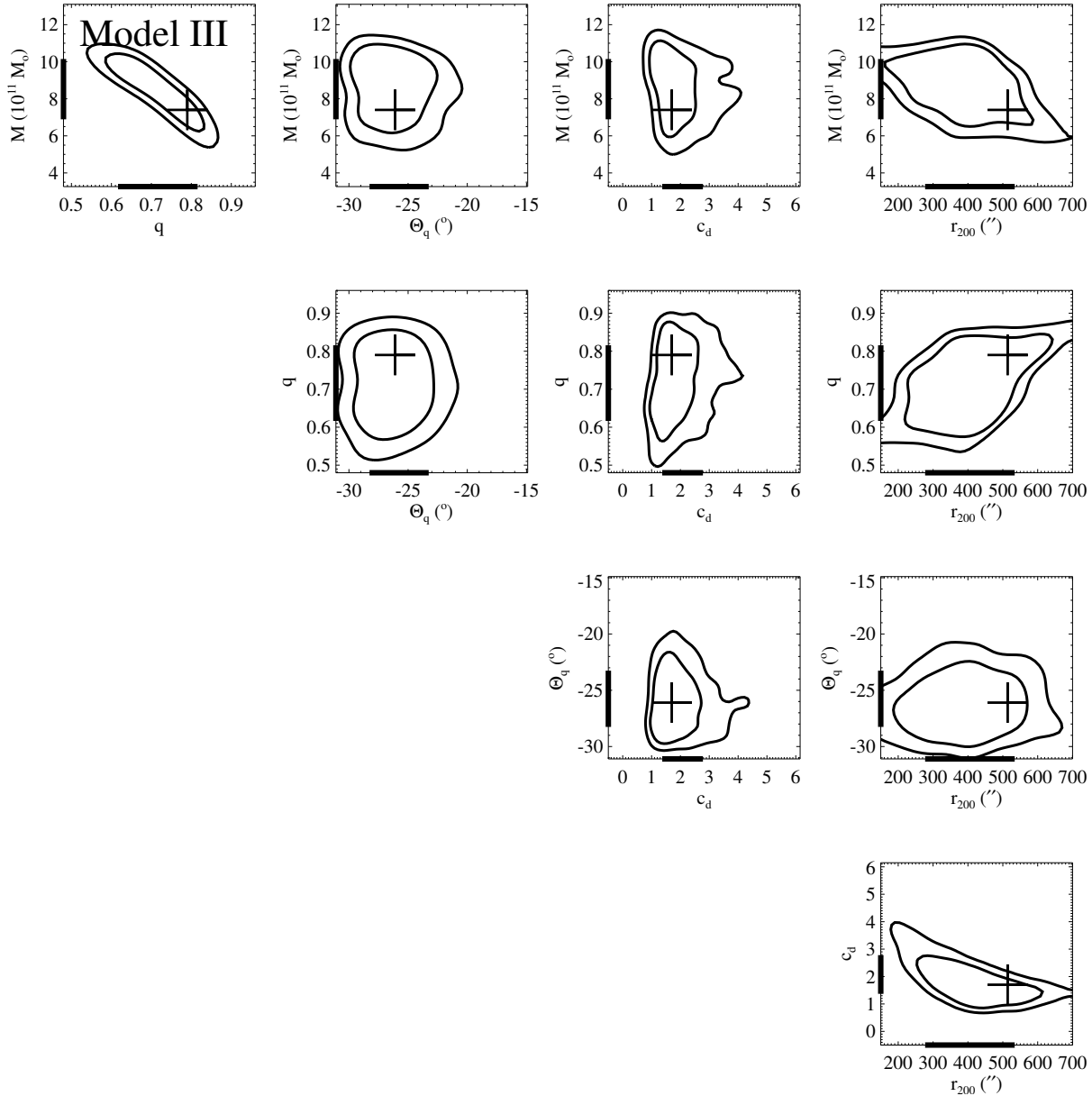


Figure 7. Error estimates of the MCMC for the NFW+de Vaucouleurs model (Model III), plotted are the 68 and 90 % confidence regions of the distribution. The crosses mark the minimum- χ^2 value from Table 5. The bars on the axes mark the respective 68 % marginalised error intervals. The individual points of the MCMC are omitted for clarity.

There $\rho_c(z)$ denotes the critical density of the universe at redshift z and σ_{group} the velocity dispersion of the group. Subsequently this gives an Einstein radius of $\Theta_E = 3.6 \pm 1.5''$, using again a SIS assumption (see Sec. 3.1 for details). This results in a convergence of and shear of

$$\begin{aligned} \kappa_A^{\text{SIS group}} &= 0.029 \quad , \\ \gamma_A^{\text{SIS group}} &= 0.029 \end{aligned} \quad (6)$$

at galaxy A if galaxy I is assumed to be the group centre. Alternatively, we model the smooth group as a 'typical' richness 12 galaxy group NFW (Navarro et al. (1996)) halo with concentration $c = 4.22$ and $r_{200} = 848$ kpc from Johnston et

al. (2007). We obtain a convergence and shear of

$$\begin{aligned} \kappa_A^{\text{NFW group}} &= 0.025 \quad , \\ \gamma_A^{\text{NFW group}} &= 0.026 \quad . \end{aligned} \quad (7)$$

Further, we note that the angle of A towards I is -26° , therefore forming an angle of 16° with the external shear value derived in Sec. B1. We examine the HST and SDSS frames which cover galaxy I and its vicinity for group-scale multiple images to further constrain the group mass distribution but do not find any sign for strong lensing.

Model IV : From Section 2.2 we expect that there is some environment dark matter present in this galaxy. We check whether using this group dark matter contribution with a de Vaucouleurs component for galaxy A is sufficient to ex-

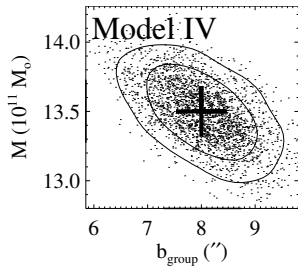


Figure 8. Error estimates of the MCMC for the de Vaucouleurs+GI model (Model IV), plotted are the individual points of the MCMC together with the 68 and 90 % confidence regions of the distribution, indicated by the density contours. The crosses mark the minimum- χ^2 value from Table 5. The bars on the axes mark the respective 68 % marginalised error intervals.

plain the observations, even though modelling this system with a pure de Vaucouleurs component fails, see Appendix A. Therefore, in this model, we combine the de Vaucouleurs profile with a group halo centred at galaxy I. To account for the environment, we include the galaxy group explicitly as a SIS profile centred at galaxy I in Table 3. We use a prior on the group Einstein radius of $b_{\text{group,prior}} = (3.6 \pm 1.5)''$. The de Vaucouleurs component has shape parameters as stated in Table 1. The group acts almost as a mass sheet. We get a $\chi^2 = 18.9$ for the best-fitting model. We get parameter estimates of $M_{\text{deV}} = (13.5^{+0.2}_{-0.2}) \times 10^{11} M_{\odot}$ and $b_{\text{group}} = (8.0^{+0.7}_{-0.7})''$ as can be seen in Fig. 8. Besides being a worse fit than most of the other models, this model also needs a much more massive group present than what is likely from the observations. Therefore, dark matter that is distributed almost uniformly within Θ_E of the galaxy does not provide a good model for the system.

Model V : This model adds environmental effects to Model III. Therefore we add the group GI explicitly as above, yielding 3 components: the group GI, the dark matter associated with the galaxy as an elliptical NFW profile and a stellar component modelled as a de Vaucouleurs profile. We use the same constraints as for Model III. We get the following parameters, see also Fig. 9: $M_{\text{deV}} = (10.4^{+1.4}_{-1.7}) \times 10^{11} M_{\odot}$, $q_d = (0.79^{+0.11}_{-0.11})$, $\Theta_q = (-21.6^{+8.8}_{-5.4})^\circ$, $c_d = (1.4^{+1.2}_{-0.4})$, $r_{200} = (321^{+141}_{-153})''$, and for the galaxy group $b_{\text{group}} = (4.9^{+1.6}_{-1.7})''$. We note that these parameter estimates do not significantly change compared to Model III, therefore the inclusion of group GI has only a small influence on the estimated galaxy parameters; the M_{deV} for the de Vaucouleurs component is slightly increased. Again, we are not able to constrain the concentration c or r_{200} of the dark matter halo. Models Va and Vb in Appendix A employ a NSIE-like galaxy dark matter halo (Model Va) and an external shear contribution instead of a explicit group contribution (Model Vb) and again give results very similar to Model V regarding the parameters for the lensing galaxy.

3.3 Full surface brightness distribution using LENSVIEW

We also use LENSVIEW (Wayth & Webster (2006)) to derive models and mass estimates for SDSSJ 1430+4105 and to reproduce the full surface distribution of the lensed galaxy

Table 6. minimum- χ^2 values derived with LENSVIEW

	b (")	q	Θ_q ($^\circ$)	γ^1	Θ_γ	β	χ^2_{red}
SIE	1.49	0.69	-19.5	0 ²	0 ²	2.00 ²	1.4
SIE+ES	1.45	0.80	-23.0	0.046	-105	2.00 ²	1.02
PL	1.53	0.77	-20.2	0 ²	0 ²	1.83	1.02
PL+ES	1.50	0.85	-22	0.047	-106	1.89	0.99

¹The external shear at the position of the galaxy A
²fixed value

and its unlensed source. LENSVIEW is a publicly available program that fits parametric lens models to image data and uses the best-fitting lens model to reconstruct the source and image. The code uses the image data, a corresponding noise map, and an image mask to minimise $\chi^2 - \lambda S$, where χ^2 is the chi square difference between the reconstructed image and the data, S is the entropy in the source, and λ is internally adjusted such that χ^2 approaches its target value. If the data are well fit by the model, the entropy term serves to smooth the source. Because the flux of each unmasked data pixel is used in the fit, LENSVIEW is well-suited to systems with extended flux like SDSS J1430+4105. The profile used here is defined, following Barkana (1998), as

$$\kappa(\Theta_1, \Theta_2) = \frac{b'}{2} \left(\frac{3 - \beta}{q} \right)^{\frac{\beta-1}{2}} (\Theta_1^2 + \frac{\Theta_2^2}{q^2})^{\frac{1-\beta}{2}}, \quad (8)$$

where b' gives the Einstein radius, q the axis ratio and β again the power law exponent of the profile. We note that the normalisation of the profiles is different from Eq. 1, resulting in different values for the Einstein radius in both approaches.

The minimum- χ^2 results are stated in Table 6. The SIE best-fitting parameter values derived here agree with those found in Sec. 3.1, when directly compared to Model I in Table 4. For the PL model, we see a consistency of the different models from GRAVLENS and LENSVIEW within the stated errors for q , Θ_q and β . Since, as mentioned before, the normalisation of the convergence profiles is different, the b / b' values do not compare directly to each other. For the models including the environment, the direct comparison of the SIE+ES model with Model Ia shows again a consistency within the errors derived in Appendix A for the lens parameters. However, the external shear angle shows a discrepancy, the angle is offset relative to the expected value derived in Sec. 2.2. Since the external shear contributes no mass, this will not have a significant effect on the mass estimates in Sec. 4. The same is true for the PL+ES case, the comparison with Model IIa gives an agreement within the given errors in all parameters besides Θ_γ .

3.4 Tests on the strong lensing assumptions

For all but the single, pure de Vaucouleurs model, the centre of the light and mass distribution do not necessarily have to coincide. To address possible systematic effects of the assumption that the mass model profiles are centred on the centre of light, we use Model I with a free centre with priors on the centre position of uncertainty $\sigma_{\Theta_{1,1}} = \sigma_{\Theta_{2,1}} = 0.2''$. In this case, we find: $b = (1.51^{+0.02}_{-0.02})''$, $q = (0.69^{+0.06}_{-0.04})$ and

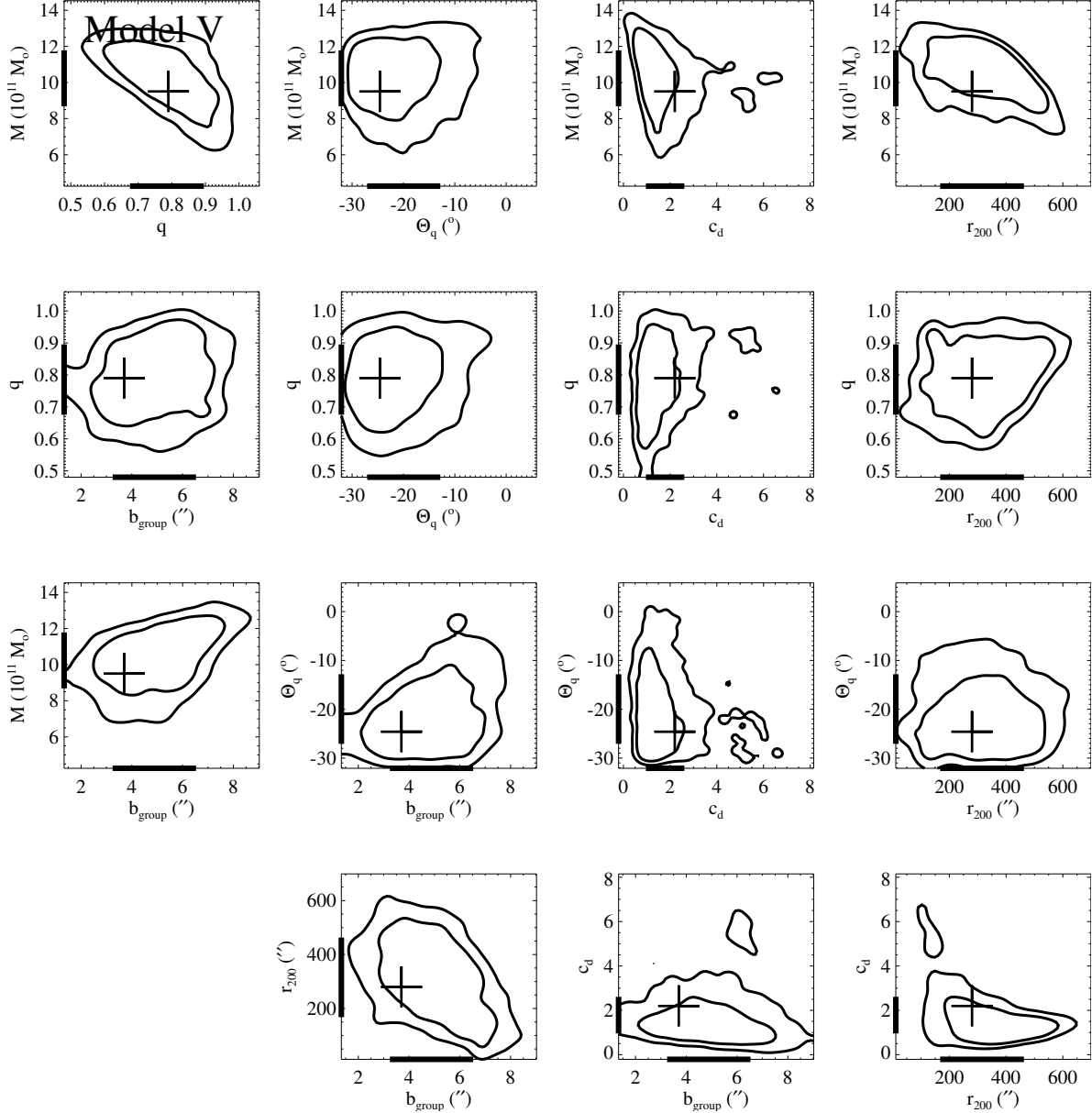


Figure 9. Error estimates of the MCMC for the de Vaucouleurs+NFW model (Model V), plotted are the 68 and 90 % confidence regions of the distribution. The crosses mark the minimum- χ^2 value from Table 5. The bars on the axes mark the respective 68 % marginalised error intervals. The individual points of the MCMC are omitted for clarity.

$\Theta_q = (-26.1^{+2.3}_{-2.4})^\circ$. The lens total mass centre moves to $\Theta_{1,1} = (-0.02^{+0.05}_{-0.07})''$ and $\Theta_{2,1} = (-0.11^{+0.04}_{-0.04})''$. The lensing strength b and the axis ratio q agree within the errors with the values derived for Model I, but the uncertainty on q increases. While the lens position $\Theta_{1,1}$ is still consistent with 0, there is a dependency of $\Theta_{2,1}$ and Θ_q . This has no effect on the mass profiles $M(< R)$, so we conclude that we can fix the lens total mass centre to its centre of light without inducing systematic effects on the derived masses.

In the previous sections we restricted the smooth mass model of the group GI to be spherically symmetric. We alter the shape of GI to an elliptical isothermal profile (SIE) and study the changes on the best-fitting SIE lens models. This model is analogous to Model Ia, but combines a SIE lens with a SIE instead of a SIS galaxy group centred

on galaxy I. Therefore, we create 2000 random representations of GI as a SIE. For each of these representations, the axis ratio is randomly chosen between $q_{GI} = [0.6, 1]$ with a random orientation. The centre of this SIE group model is taken from a gaussian distribution, centred on galaxy I, with a width of $\sigma_{x,GI} = \sigma_{y,GI} = 1.5''$. We recalculate the best-fitting parameters for each of these SIE+GI(SIE) models and evaluate the scatter of the best-fitting parameters to estimate the systematic uncertainties emerging from the assumption of a simple SIS group halo. This results in 68% c.l. distributions of the best-fitting parameters for this modified Model Ia: $b_{\text{lens}} = [1.44, 1.46]''$, $q_{\text{lens}} = [0.79, 0.82]$, $\Theta_q = [-18.4, -16.2]^\circ$ and $b_{\text{group}} = [4.27, 4.42]''$. These intervals are small compared to the statistical uncertainties for Model Ia derived from the MCMC sampling. We conclude

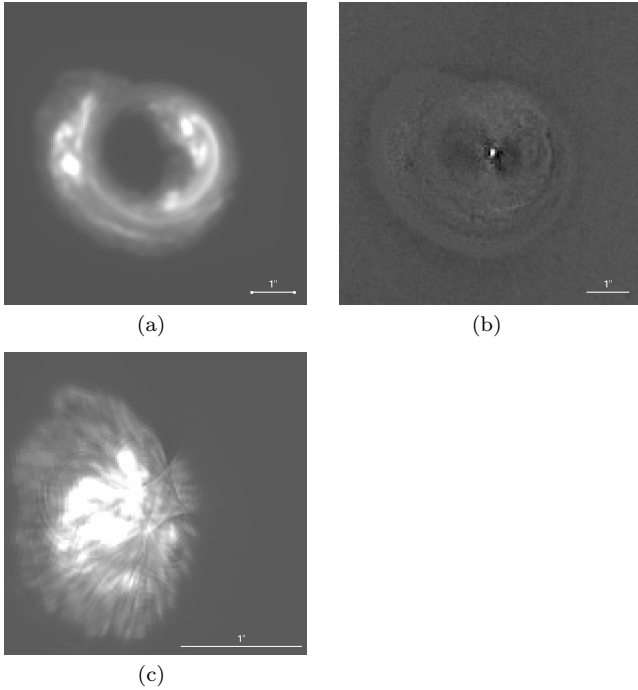


Figure 10. best-fitting model for the SIE case 10(a), its residuals 10(b) and the corresponding source 10(c). For the images 10(a) and 10(b), the pixel size is the same as in Fig. 2; the source has a 3 times smaller pixel size. The same flux scaling has been used on all images.

that the details of the group model representation do not change the results for the lensing galaxy significantly, therefore including the most simple SIS model for GI is sufficient.

4 RESULTS FOR THE GALAXY MASS PROFILE

The total masses $M(< R)$ within a cylinder of radius R and its derivatives obtained from the SL analysis for Models I to V are shown in Figs. 12 and 13. We have calculated these values within several concentric apertures with radii $([0.46 \ 0.92 \ 1.26 \ 1.59 \ 1.95 \ 2.32 \ 2.78] \text{''})$, chosen to lie in the radial regions covered by the lensed images plus extrapolations towards smaller / larger radii. For the Models I to V of Secs. 3.1 and 3.2, the masses are estimated by randomly taking 1000 MCMC points and creating convergence maps for each one of these 1000 models. The 68 % (90 %) errors are estimated by taking the central 680 (900) models at each radius.

4.1 Mass profiles for the single component isothermal and powerlaw models

First we focus on the masses derived for Models I and II in Table 4. The Einstein radii are defined as the radii within which the mean convergence equals 1. For this, we calculate the mean convergence around the Einstein radius in $0.03''$ distance bins. The results of this calculation are stated in Table 7. Since all models agree on an Einstein radius of $\Theta_E = 1.51'' \cong 6.48 \text{ kpc} = R_E$, we adopt this

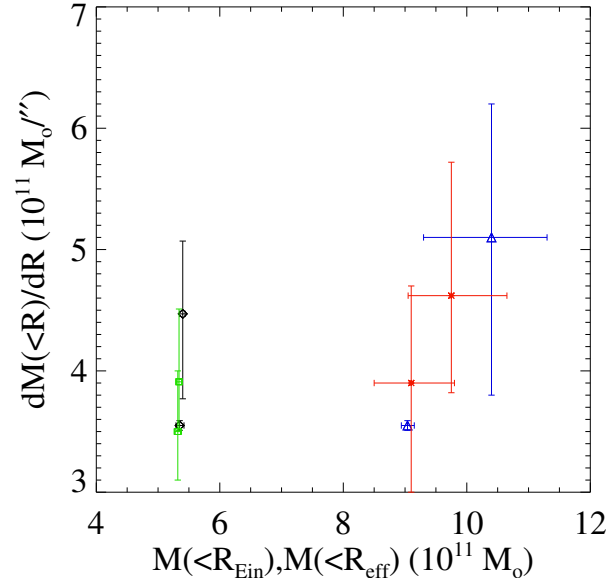


Figure 11. The masses and radial derivatives for the Models stated in Table 7 and Table 8. Plotted are the mean values together with its 1σ error bars. For Models I and II, the black asterisks mark the values at the Einstein radius (fixed to $1.51''$), while the blue triangles mark the extrapolations to the effective radius of the galaxy. For the de Vaucouleurs like models II and V, the green squares are the values at the Einstein radius, the red crosses are the ones at the effective radius. While the total mass within the Einstein radius is tightly constrained independent of the model used, the mass within the effective radius depends on the mass model used.

value as “the” Einstein radius of this lens with an uncertainty of $0.03'' \cong 0.13 \text{ kpc}$. We get a mean Einstein mass of $(5.37 \pm 0.06) \times 10^{11} M_{\odot}$ for the Models I and II with a fixed Einstein radius of $\Theta_E = 1.51''$. This values are in good agreement with the ones stated by Auger et al. (2009) for this system also based on strong lensing.

We also extrapolate the models to the effective radius $r_{\text{eff}} = 2.55'' \cong 10.96 \text{ kpc}$ of the galaxy, and calculate the mass and its derivative. We find an enclosed mass between $M_{\text{tot,enc}} = 8.9 \times 10^{11} M_{\odot}$ and $M_{\text{tot,enc}} = 11.3 \times 10^{11} M_{\odot}$ on a 1σ level, depending on the model used. The azimuthally averaged results of the included masses are plotted in Fig. 12. For an SIE model, the mass included within radius r grows linearly with the radius, so the derivative of it is expected to be independent of the radius. This is the case for the singular isothermal model (Model I) in Table 4. If we allow the steepness to vary (Model II) the mass profile tends to be steeper at the Einstein and effective radius. For the radial mass derivative at the Einstein radius, we calculate values between $\frac{dM_{\text{tot,enc}}}{dR} = 0.8 \times 10^{11} M_{\odot} \text{ kpc}^{-1}$ and $\frac{dM_{\text{tot,enc}}}{dR} = 1.2 \times 10^{11} M_{\odot} \text{ kpc}^{-1}$. The extrapolation to the effective radius ranges from $\frac{dM_{\text{tot,enc}}}{dR} = 0.8 \times 10^{11} M_{\odot} \text{ kpc}^{-1}$ for Model I to $\frac{dM_{\text{tot,enc}}}{dR} = 1.6 \times 10^{11} M_{\odot} \text{ kpc}^{-1}$ for Model II. This values are plotted in Fig. 11. Here and in Table 4 we state the 68 % c.l. errors.

Table 7. The masses and mass derivatives at the Einstein radius, the globally adopted Einstein radius and the effective radius for the different models. Given are the projected, enclosed masses and its derivatives

Model	Θ_{Ein} (")	M_{Ein} $10^{11} M_{\odot}$	$\frac{dM}{d\Theta}(\Theta_{\text{Ein}})$ $10^{11} M_{\odot}/''$	κ_{Ein}	$M(< 1.51'')$ $10^{11} M_{\odot}$	$\frac{dM}{d\Theta}(\Theta = 1.51'')$ $10^{11} M_{\odot}/''$	$M(< 2.55'')$ $10^{11} M_{\odot}$	$\frac{dM}{d\Theta}(\Theta = 2.55'')$ $10^{11} M_{\odot}/''$
Model I	1.51 ± 0.03	$5.35^{+0.07}_{-0.06}$	3.55 ± 0.04	$0.497^{+0.006}_{-0.005}$	$5.35^{+0.07}_{-0.06}$	3.55 ± 0.04	$9.04^{+0.11}_{-0.10}$	3.55 ± 0.04
Model II	1.54 ± 0.03	$5.54^{+0.06}_{-0.05}$	$4.5^{+0.6}_{-0.8}$	$0.68^{+0.08}_{-0.10}$	$5.40^{+0.04}_{-0.05}$	$4.5^{+0.6}_{-0.7}$	$10.4^{+0.9}_{-1.1}$	$5.1^{+1.1}_{-1.3}$

¹galaxy part only, mass contribution of GI is ignored

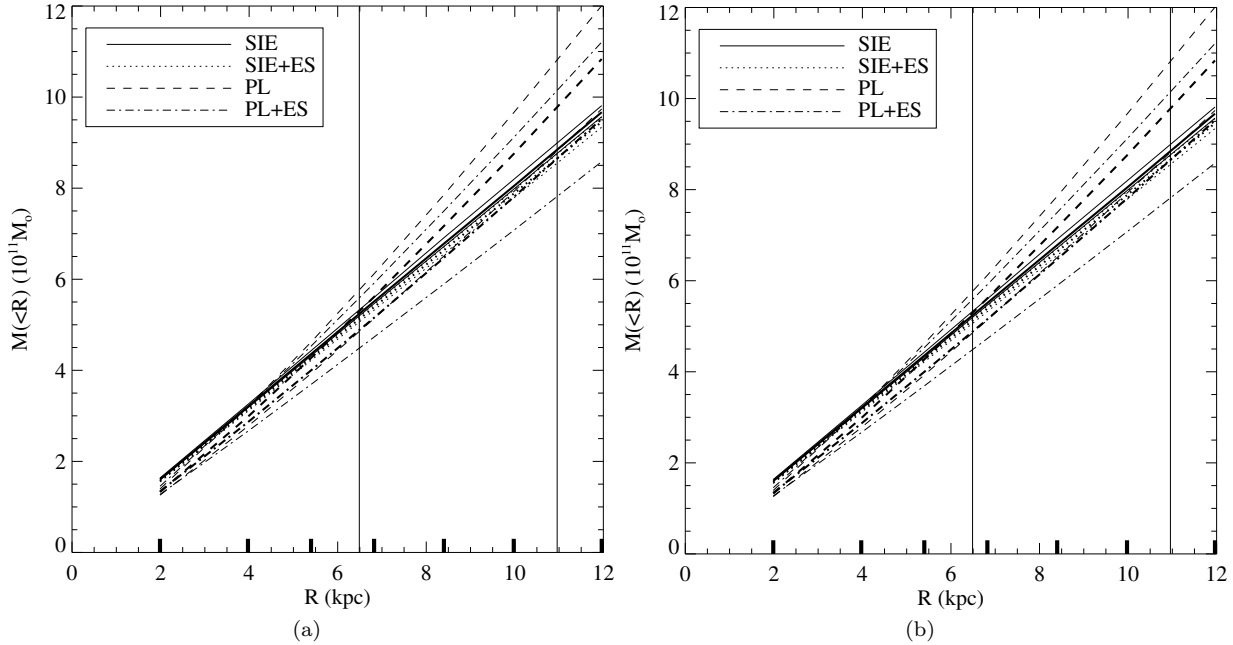


Figure 12. The mass within radius R , $M(< R)$, from the models I and II, analysed in Sec. 3 is plotted in Fig. 12(a). For each model, 1000 random entries from the MCMC are used to calculate the errors. Each time, the means and 90 % errors are shown, with the respective means in bold lines. The bars at the bottom mark the radii of the apertures used to calculate the enclosed projected masses. The masses are in units of $10^{11} M_{\odot}$, the radii are stated in kpc in the lens plane. The mass estimates for the Models I and II are shown as solid (I) and dashed (II) lines. Vertical lines indicate the Einstein and effective radius in both plots. Fig. 12(b) shows the same as Fig. 12(a) but for the LENSVIEW derived masses. The errors are estimated by an increase of the reduced χ^2 of the extended model by 1. As can be seen, the masses agree with each other in terms of derived masses within the errors.

4.2 Mass profiles for the de Vaucouleurs plus dark matter halo models

From the single component lens analyses in Sec. 4.1, we conclude that the total projected mass density profile is isothermal or slightly shallower than isothermal. The de Vaucouleurs mass density drops faster with radius than the isothermal profile. Therefore, we expect the pure de Vaucouleurs profile to be a poor description of this lens' mass profile (as seen in Model IV in Sec. 3.2 and Model IVa in Appendix A) and expect that we need to add some component which follows a shallower than isothermal density profile. In principle a constant mass sheet, like a nearby group halo would approximately provide, could do this, given that it provides enough mass at the position of the lens. In Model IV, we see that this model is a poor fit to the data. Therefore a (dark) matter component centred at the position of the lens is necessary. We model this in Models III, IIIa and IIIb in Sec. 3.1 and Appendix A with different types of dark mat-

ter halo profiles. A SIE-like dark matter component (Model IIIa) suppresses the de Vaucouleurs part of the matter profile, effectively yielding a single component model. Because the light distribution is well-fit by a de Vaucouleurs profile, we require a non-zero de Vaucouleurs component for this 2 component fit, hence we do not consider Model IIIa in the following. The Models IIIb, Va and Vb in Appendix A give similar results to Models III and V in Sec. 3.1. Therefore, in the following, we mostly consider Models III and V, which model the lens using an NFW profile for the dark matter component.

Besides the stars and the dark matter, an elliptical galaxy or a galaxy group also contains some amount of gas. Since we do not model this component individually, this gas needs to be incorporated in either the dark matter or the de Vaucouleurs component, effectively limiting the accuracy of our mass estimates to the gas mass fraction in elliptical galaxies and groups of galaxies. Young et al. (2011) get typical molecular gas masses of early-type galaxies in the ATLAS^{3D}

project of $M(\text{H}_2) \leq 10^9 M_\odot$, less than 1% of the total galaxy masses derived here. The hot gas component in an elliptical galaxy or a group of galaxies can contribute up to 10% of the total mass in the centre of the galaxy or group of galaxies, see e.g. Sanderson et al. (2003). Hence the uncertainty of our mass estimates due to the neglected gas is $\approx 10\%$.

We again adopt $\Theta_E = 1.51''$ for the Einstein radius. First we focus on the masses within this radius, see Table 8. For the total masses within the Einstein radius of the models III and V, we measure $M_{\text{tot,Ein}} = (5.33 \pm 0.04) \times 10^{11} M_\odot$. The radial mass derivative is $\frac{dM_{\text{tot,enc}}}{dR} = 0.86_{-0.07}^{+0.09} \times 10^{11} M_\odot \text{kpc}^{-1}$. The extrapolations to the effective radius give $M_{\text{tot,eff}} = 9.5_{-0.5}^{+0.6} \times 10^{11} M_\odot$ for the mass and $\frac{dM_{\text{tot,enc}}}{dR} = 1.00_{-0.14}^{+0.16} \times 10^{11} M_\odot \text{kpc}^{-1}$ for its derivative. This values are plotted in Fig. 11. As can be seen, the enclosed masses and its derivatives at the Einstein radius and the effective radius agree with each other throughout Models I, II, III and V. We state the de Vaucouleurs mass within the Einstein and effective radius of Model III as Component IIIA in Table 8. We get a mass of $M_{\text{deV,Ein}} = (3.2_{-0.7}^{+0.5}) \times 10^{11} M_\odot$, meaning that $\frac{M_{\text{deV,Ein}}}{M_{\text{deV,tot}}} \approx 35\%$ of the total de Vaucouleurs mass is concentrated within the Einstein radius for this lens. For Model V, we get similar values for the de Vaucouleurs component, see Component VA in Table 8. In Fig. 13 and Fig. A3 in Appendix A, the projected, enclosed lens masses and their derivatives are plotted versus radius for the different 2 component strong lensing models. The measurements are done using circular apertures, so all of these values are azimuthally averaged. As one can see, including an explicit group halo at GI (Model V) has only a minor influence on the mass estimates and their derivatives. The total masses agree very well with the one component estimates in Fig. 12. Also, all models agree very well on the total masses and their radial derivatives, tending to give a shallower than isothermal mass profile in the centre. For the Models III and V in Fig. 13, the dark matter haloes modelled as NFW-haloes agree very well with each other, meaning that the environment has only minor influence on the mass estimates. This is also true for the de Vaucouleurs component. We note that the uncertainties on the individual components are larger than the uncertainties on the total masses and derivatives, giving a well-constrained total mass.

4.3 3d spherical reconstruction

Further, we also reconstruct the 3d matter densities from the 2d data for Model III. For this, we employ the inverse Abel-transform:

$$\rho(r) = -\frac{1}{\pi} \int_r^\infty \frac{d\Sigma}{dR} \frac{dR}{\sqrt{R^2 - r^2}}, \quad (9)$$

transforming a 2d circular density function Σ into a 3d spherical density function ρ . Since this only transforms circular to spherical profiles and vice versa, we start from the mass measurements within a cylinder in Fig 13(a) for the azimuthally averaged profile. In Eq. 9 the integration extends to infinity, which is not possible due to our limited range of reliable data. To estimate the radial range at which we can use Eq. 9 only integrating up to our last data bin we test it on a SIS toy model. For a SIS toy model, we know both the spherical and the projected circular density. We then con-

sider this radial range reliable where the deviation of the reconstructed 3d density from the analytical SIS density does not exceed $2 \times 10^7 M_\odot \text{kpc}^{-3}$. From this comparison, we conclude that this inverse Abel transformation is only reliable up to ≈ 6.5 kpc with a systematic error smaller than 30%, given our limited radial range of data. The reconstructed 3d profile is shown in Fig. 14. The errors plotted are only statistical, not taking any systematic effects into account. The dark matter accounts for only a minor fraction of the total mass in the 3d centre of the galaxy. We now turn to Fig. 7 in Thomas et al. (2011). In the lower part of Fig. 7 they have displayed the ratios of the mean dark matter density and mean total density within the Einstein radius of Coma galaxies as a function of their velocity dispersion. (For the definition of the synthetic Einstein radius for Coma galaxies, see Thomas et al. 2011). To see whether there are structural differences for the Coma and the higher redshift SLACS sample one would like to enter the corresponding deprojected values for SLACS galaxies in these figures as well. These were not available until now because the dark to total matter fractions were only calculated for the line of sight projected densities within the Einstein radii (i.e. cylindrical averages) by gravitational lensing. The corresponding projected values are shown for SLACS (and Coma) galaxies in the upper part of Fig. 7 of Thomas et al. (2011). The projected and deprojected values differ, since the projection along the line of sight mixes scales: Parts of the matter that has a large physical distance from the centre of the galaxy but lie on the line of sight are taken into account when calculating the projected dark matter fractions. Due to the monotonic increase of the dark to total matter density ratios as a function of radius, the projected ratios displayed in the upper part of Fig. 7 of Thomas et al. (2011) are upper limits to the central, 3-dimensional density ratios at the Einstein radius. With the analysis described in this work we are able to measure the 3-dimensional densities of the (spherically averaged) dark matter and de Vaucouleurs components of the lensing galaxy separately from gravitational lensing alone due to the large radial coverage of multiple images in the image plane by one source. Since the source is only one background object, we do not need to take the systematic uncertainties into account that arise in systems with multiple image systems from sources at different redshifts like e.g. Gavazzi et al. (2008). At the Einstein radius we obtain (using Fig. 14, displaying Model III (de Vaucouleurs+NFW)) a dark to total density ratio of 22 % for the dark to total density. Doing the same for the Model V where SDSSJ 1430+4105 (consisting of de Vaucouleurs and dark matter component) is embedded in a DM halo centred on galaxy I we find that the ratio of dark to total matter density at the Einstein radius is about 14%. Since the dark matter fraction increases towards the outskirts, these ratios of densities at the Einstein radius are upper limits for the mean dark matter to total matter density ratios of galaxy SDSSJ 1430+4105 within the same Einstein radius. On a (90% c.l.) basis, the density ratios at the Einstein radius are larger than 15% (Model III) and 5 % (Model V) for the dark to total matter density.

Table 8. Same as Table 7 for the 2 component models.

Model	Θ_{Ein} (")	M_{Ein} $10^{11} M_{\odot}$	$\frac{dM}{d\Theta}(\Theta_{\text{Ein}})$ $10^{11} M_{\odot}/''$	κ_{Ein}	$M(< 1.51'')$ $10^{11} M_{\odot}$	$\frac{dM}{d\Theta}(\Theta = 1.51'')$ $10^{11} M_{\odot}/''$	$M(< 2.55'')$ $10^{11} M_{\odot}$	$\frac{dM}{d\Theta}(\Theta = 2.55'')$ $10^{11} M_{\odot}/''$
Model III	1.51 ± 0.03	5.34 ± 0.05	$3.9^{+0.6}_{-0.4}$	$0.55^{+0.08}_{-0.06}$	5.34 ± 0.05	$3.9^{+0.6}_{-0.4}$	$9.8^{+0.9}_{-0.7}$	$4.6^{+1.1}_{-0.8}$
Component IIIA ¹					$3.2^{+0.5}_{-0.7}$	$1.4^{+0.2}_{-0.3}$	$4.4^{+0.7}_{-1.0}$	$0.90^{+0.15}_{-0.20}$
Model V	1.48 ± 0.03	5.21 ± 0.06	3.5 ± 0.4	0.50 ± 0.06	5.32 ± 0.06	$3.5^{+0.5}_{-0.4}$	$9.1^{+0.7}_{-0.6}$	$3.9^{+0.8}_{-0.9}$
Component VA ¹					$3.8^{+0.5}_{-0.6}$	$1.6^{+0.2}_{-0.3}$	$5.2^{+0.7}_{-0.8}$	$1.06^{+0.15}_{-0.17}$
Component VB ²	1.45 ± 0.03	$4.91^{+0.09}_{-0.08}$	$3.2^{+0.5}_{-0.4}$	$0.47^{+0.07}_{-0.06}$	$5.11^{+0.10}_{-0.09}$	3.2 ± 0.5	$8.5^{+0.8}_{-0.7}$	$3.3^{+1.1}_{-0.8}$

¹de Vaucouleurs like part only, dark matter contribution is ignored

²galaxy part only, mass contribution of GI is ignored

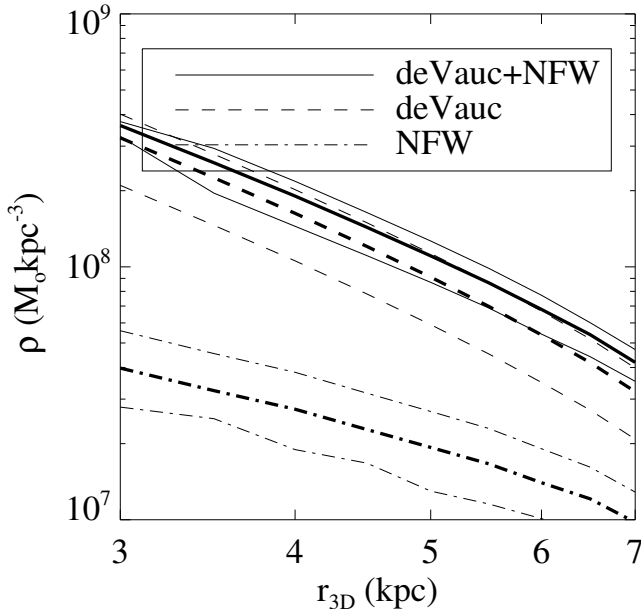


Figure 14. The 3d densities for the stellar (dashed) and the dark (dash-dotted) component, as well as the total matter (solid) For this, the data of Model III is used. Plotted are the median (thick) and the 90 % c.l. intervals. Spherical symmetry is assumed for this reconstruction.

5 MASS TO LIGHT RATIOS FOR THE DE VAUCOULEURS COMPONENT AND DARK TO TOTAL MASS RATIO

Since we calculated the de Vaucouleurs masses for this galaxy, we now want to estimate the rest frame mass to light ratios of this galaxy. Further, we evolve this mass to light ratios to present day values in order to compare it with Coma galaxies. First, we calculate the dark matter fractions within the Einstein radius. In Fig. 15, we plot the dark over total enclosed mass fraction within the Einstein radius. The error bars are estimated as before from the central 68 % and 90 % entries of the random sample drawn from the MCMC for Models III and V, respectively. The fractions for Model III and V are: $\frac{M_{\text{NFW}}}{M_{\text{tot}}} = (0.40^{+0.13}_{-0.09})$ and $\frac{M_{\text{NFW}}}{M_{\text{tot}}} = (0.27^{+0.12}_{-0.11})$. These fractions indicate a substantial amount of dark matter within the Einstein radius of this lens. As can be seen, this picture is not significantly altered by locating the group at GI in Model V. Although the actual numbers change, we still need dark matter associated with the lens in the centre

of the galaxy. Since we ignore the dark matter contribution associated with the group GI in Model V for the total mass, we get a lower dark matter fraction for Model V compared to Model III.

For the Models III and V, we calculate the mass to light ratios for the de Vaucouleurs component at the redshift of the lens. We use the masses from lensing and the light (in rest frame B and R) as obtained from photometric data. To compare the mass to light ratios with present day galaxies, we also need the luminosity evolution to redshift zero in these bands. We take the observed *griz* SDSS photometry for this system which covers the rest frame B and R filters to calculate the B-R rest frame colour.⁶ We calculate a colour of $(B - R) = (0.80 \pm 0.03)$ and luminosities of $L_{\text{B,rf}} = (1.66 \pm 0.03) \times 10^{11} L_{\odot}$ and $L_{\text{R,rf}} = (1.92 \pm 0.02) \times 10^{11} L_{\text{R},\odot}$ from the absolute rest frame magnitudes. To estimate the luminosity evolution until today, we fit 3 extinction-free BC (Bruzual & Charlot 2003) composite stellar population (CSP) models to the observed *griz* SDSS photometry: A Salpeter initial mass function (IMF) (Salpeter 1955) with solar metallicity (Model A) and 2 models with Chabrier IMF (Chabrier 2003) and solar / super-solar metallicity (Models B,C), respectively, see Drory et al. (2001, 2004). The best-fitting results are stated in Table 9 together with the luminosity evolutions in B and R bands and the best-fitting stellar masses, which agree with Grillo et al. (2009). From the best-fitting star formation histories (SFH) to the spectral energy distribution (SED) we obtain a stellar age of typically 8 Gyrs and a B-R colour of 0.8. Therefore, this galaxy has a formation redshift of approximately 2 to 3 which is a typical value for elliptical galaxies. If we divide the de Vaucouleurs masses derived by lensing in Sec. 3 by the luminosities derived from the SDSS photometry we obtain the mass to light ratios (MtoL) for the de Vaucouleurs component of this galaxy. For Models III and V, we find a MtoL of $\frac{M_{\text{deV}}}{L_{\text{B}}} = (5.3^{+0.8}_{-1.1}) \frac{M_{\odot}}{L_{\odot,B}}$ and $\frac{M_{\text{deV}}}{L_{\text{R}}} = (6.2^{+0.9}_{-1.0}) \frac{M_{\odot}}{L_{\odot,B}}$ in the B-band rest frame at the redshift of the lens. These two Models give the same MtoL within the errors, although including the group GI explicitly increases the most-likely MtoL. We compare this with the total light of the galaxy and the stellar mass derived in Grillo et al. (2009), who use composite stellar population models with a Salpeter or Chabrier IMF, a delayed exponential star formation history, and solar metallicity to model the SDSS multi band pho-

⁶ All magnitudes are given in AB.

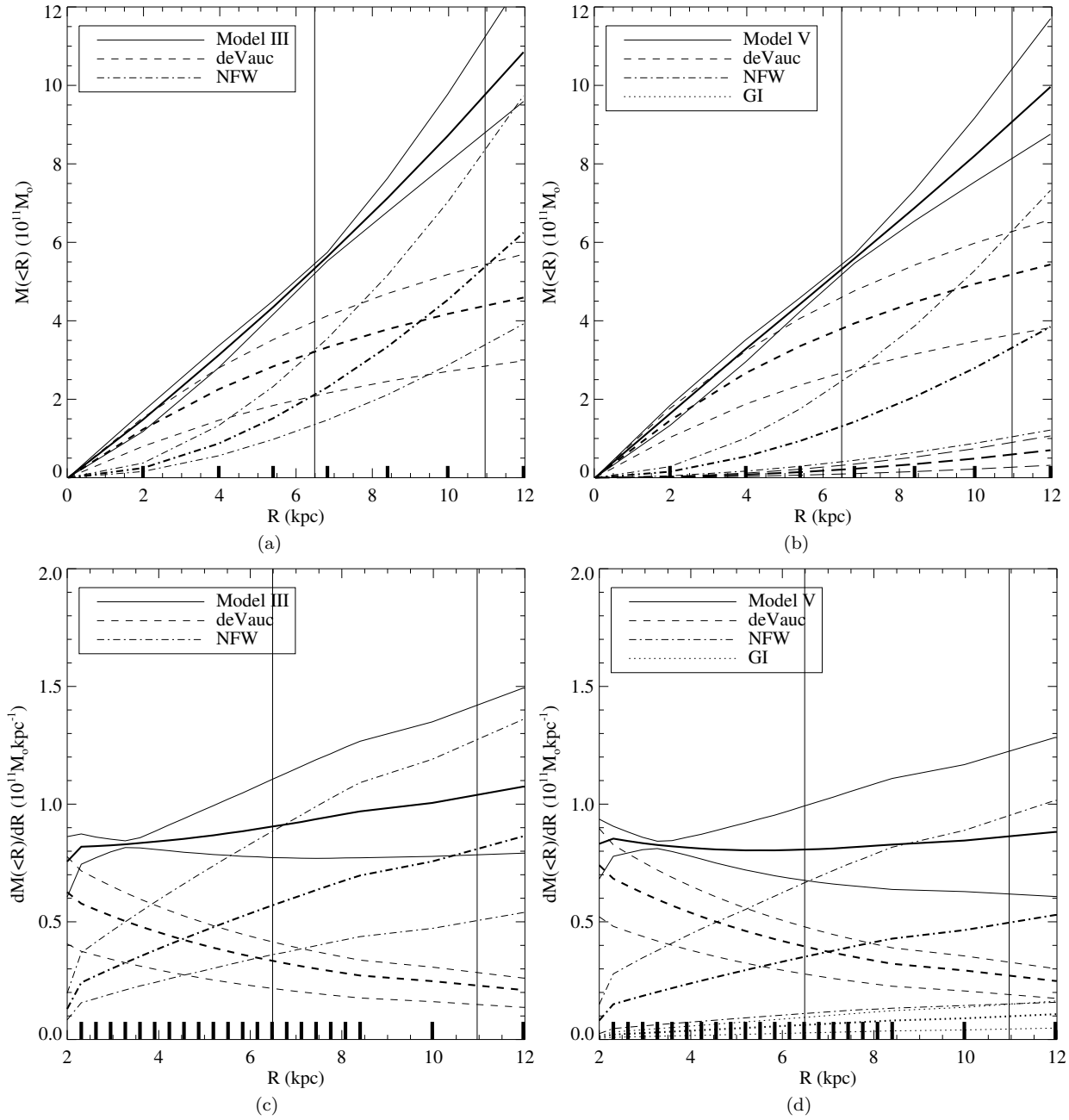


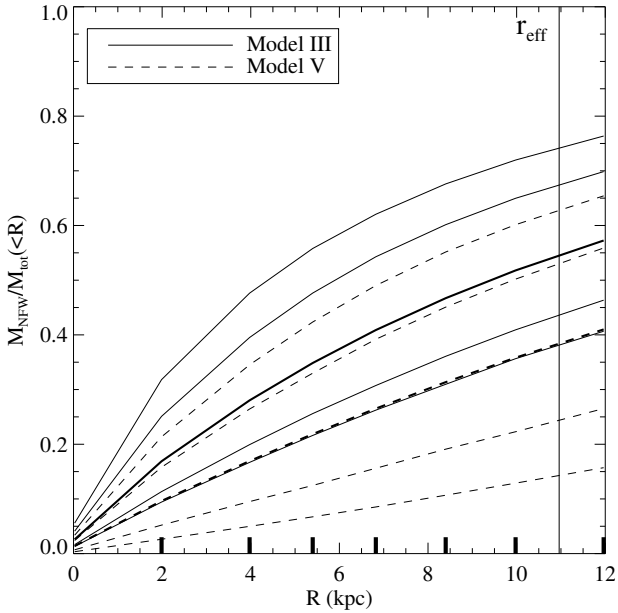
Figure 13. The mass within radius R , $M(<R)$ from the Models III and V analysed in Sec. 3. For each model, 1000 random entries from the MCMC chains are used to calculate the errors. All errors plotted are the 90 % error intervals with the respective means in bold symbols. The bars at the bottom mark the radii of the apertures used to calculate the enclosed projected masses or its derivatives. The masses are in units of $10^{11} M_{\odot}$, the radii are stated in kpc in the lens plane. In 13(a), the mass estimates of Model III for the de Vaucouleurs (dashed), NFW (dash-dotted) and its sum (solid) are plotted. While the sum of these two is fairly well constrained, the errors on the individual parts are bigger. In 13(b), the same mass estimates are plotted for Model V, together with its 90 % error intervals, splitted in de Vaucouleurs (dashed), NFW (dash-dotted) and GI (dotted) parts and its total sum (solid). The radial mass derivatives are plotted in 13(c) for Model III and 13(d) for Model V, keeping the line coding. Plotted is the change in enclosed mass with radius. This can also be interpreted as the mass in a thin ring with width dR at radius R , $M(R)$. Again, vertical lines indicate the Einstein and effective radius in both plots.

tometry. First, we compare in the rest frame B band. In Fig. 16 we plot the cumulative distribution function for the stellar mass to light ratios derived from the respective de Vaucouleurs parts of the Models III and V and Models IIIb and Va from Appendix A. We overplot the stellar MtoL ratios derived in Grillo et al. (2009) for this system and get

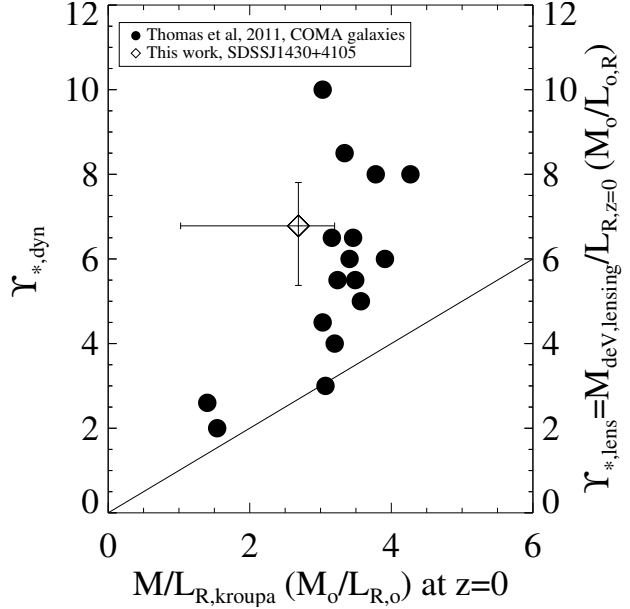
the best agreement for a NFW like halo and a Salpeter IMF. In the R-band, we get a MtoL for Models III and V of $\frac{M_{\text{deV}}}{L_{\text{R}}} = (4.6^{+0.8}_{-1.1}) \frac{M_{\odot}}{L_{\odot, \text{R}}}$ and $\frac{M_{\text{deV}}}{L_{\text{R}}} = (5.4^{+0.7}_{-0.9}) \frac{M_{\odot}}{L_{\odot, \text{R}}}$. To compare the lensing galaxy SDSSJ 1430+4105 with present day Coma galaxies (Thomas et al. 2011) we have to account for the luminosity evolution between redshift 0.285 and now.

Table 9. Galaxy luminosity evolution factors for the different IMF and metallicity models

	$(B - R)_{\text{rf}}$	T	τ	$\frac{L_{B,\text{rf}}}{L_{B,z=0}}$	$\frac{L_{R,\text{rf}}}{L_{R,z=0}}$	M_{\star}
	ABmag	Gyrs	Gyrs			($10^{11}M_{\odot}$)
A	0.77	8	2	1.77	1.48	6.7
B	0.85	8	2	1.92	1.55	4.4
C	0.81	9	2	1.66	1.42	4.0

**Figure 15.** Dark over total enclosed mass ratio for this galaxy. Shown are Models III (solid) and V (dashed). For Model V the group contribution is ignored, meaning that we only consider the dark matter associated with the galaxy itself as dark matter and only the sum of de Vaucouleurs and dark matter as the total matter. The vertical line indicates the effective radius of the galaxy. As one can see, both models predict dark matter contributions in the centre of this galaxy, with changing amounts depending on the modelling details. Plotted are the 68 % and 90 % errors, respectively.

We use the average evolution factor from the SFH models stated in Table 9, derived from the extrapolations of the fitted SFH models to redshift 0, which increases the MtoL in the R band by a factor of 1.48 for $z=0$, giving $(\frac{M_{\text{deV}}}{L_{\text{R}}})_{\text{pres}} = (6.8^{+1.2}_{-1.6}) \frac{M_{\odot}}{L_{\odot,R}}$ and $(\frac{M_{\text{deV}}}{L_{\text{R}}})_{\text{pres}} = (8.0^{+1.1}_{-1.3}) \frac{M_{\odot}}{L_{\odot,R}}$ for Models III and V, respectively. In Fig. 17, we plot this R-band de Vaucouleurs mass to light ratio at redshift zero against the present day R-band mass to light ratio for a Kroupa-IMF (Kroupa 2001), obtained again from the SFH fit of Grillo et al. (2009), translated to R-band and evolved to redshift zero. We added the results for a dynamical study of Coma galaxies by Thomas et al. (2011). This allows us to conclude that SDSSJ 1430+4105 evolves into a galaxy with mass to light ratio similar as the Coma galaxies, and shows the same conflict with respect to a Kroupa IMF as they do. This conflict to a Kroupa IMF would be resolved if, for example, the de Vaucouleurs component is not made of stars only but contains dark matter as well.

**Figure 17.** MtoL in R from lensing versus stellar mass using a Kroupa-IMF, see Grillo et al. (2009). Both values are evolved passively to the redshift 0. The lensing estimate is taken from Model III. The black points show the mass to light ratios derived from stellar dynamics analysis of the COMA cluster galaxies versus their stellar MtoL ratio derived from photometry for a Kroupa IMF, taken from Thomas et al. (2011). The solid line marks the one to one correspondence.

6 DISCUSSION AND CONCLUSIONS

In this paper, we studied the lensing properties of SDSS J1430+4105. From the complex source, we identified 5 double image systems, spanning a radial range from below $0.9''$ to almost $2.1''$. The source is spectroscopically confirmed at a redshift of 0.575. Parametric models can match the observed image positions well with an average scatter in the position comparable to the pixel size of the ACS camera input image, which is $0.05''$. Our results are:

I) The best-fitting reconstruction of the profile favours a profile slope shallower than isothermal for the best-fitting model. However, profiles with free slope for the density steepness are consistent with an isothermal profile at 90% c.l. This is also true when combining an explicit model for the de Vaucouleurs-like light distribution with a NFW-like dark matter component. Auger et al. (2010) found a steepness for the 3d density profile for this system of $\rho \sim r^{-(2.06 \pm 0.18)}$ by using the location of the Einstein radius only and combining this with stellar dynamics, in agreement with our results for the one component powerlaw total mass distribution of $\rho \sim r^{-(1.73^{+0.21}_{-0.13})}$ within the errors.

II) The galaxy is part of a group of galaxies listed in the maxBCG cluster catalogue. Using a lens mass component following the stellar light, we can not model the strong lensing signal for this galaxy if we use this component alone or combine it with a dark matter halo not centred on SDSS J1430+4105, called galaxy A. Therefore, this leads to two possibilities: Either A is indeed the centre of the galaxy group, or the galaxy A is a satellite of this group, residing in its own dark matter halo. Since we cannot distinguish

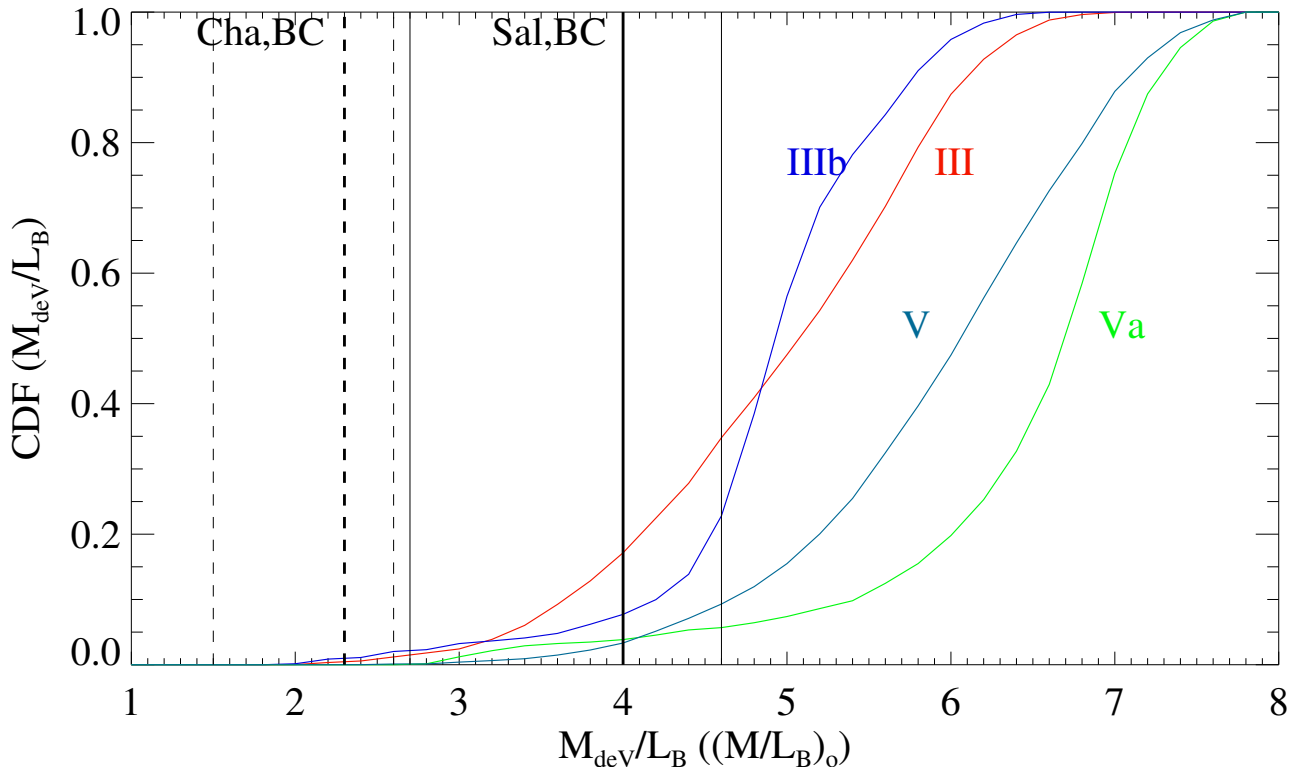


Figure 16. Cumulative probability distribution functions of the mass to light ratios for the de Vaucouleurs components of the models III and V. Models III, IIIb, V and Va are marked by red, blue, turquoise and green. The vertical lines mark the derived stellar mass to light ratios with its 1σ errors from Grillo et al. (2009) for this system fitting SFH to broad band SDSS photometry using a Salpeter IMF (solid line) and Chabrier IMF (dashed line). The mass to light ratios are as observed at $z = 0.285$ and not corrected for luminosity evolution to redshift zero.

between these 2 cases, neither from the lensing signal nor from external data, we model both scenarios and show that these lead to similar results regarding the mass distribution of the galaxy. We show that the dark matter halo of galaxy A must not be singular and isothermal at the same time, since this would suppress the de Vaucouleurs component. Both a non-singular, isothermal halo and a NFW-like halo for the dark matter halo of galaxy A fit the data well. We find agreeing dark matter fractions and distributions for both cases. From the lensing data, we cannot distinguish whether the dark matter halo follows a NFW or NSIE profile in the centre, since we cannot constrain the concentration c and r_{200} – or Θ_c for a NSIE dark matter halo – of the dark matter component well. From the models taking explicitly the environment into account we conclude that the dark matter and the light of the galaxy have the same axis ratio and are likely coaligned.

III) We estimate the rest frame B-band mass to light ratios for the lensing galaxy from the de Vaucouleurs lensing component. For the case of a deVauc+NFW mass model, we obtain a total mass of $M_{\text{deV,tot}} = (8.8^{+1.3}_{-1.9}) \times 10^{11} M_{\odot}$ for the de Vaucouleurs component. Grillo et al. (2009) have obtained stellar mass estimates for the luminous component using the ugriz broad band SDSS photometry and SFH fits. They assumed solar metallicity composite stellar populations with a delayed exponential SFH, and examined the Salpeter IMF (with BC and MAR (Maraston 2005) single stellar populations (SSP)), and the Chabrier and Kroupa IMF (based on BC-SSPs). They obtained stellar masses

of $M_{\star} = (5.6^{+0.8}_{-1.8}) \times 10^{11} M_{\odot}$, $M_{\star} = (3.9^{+1.6}_{-2.2}) \times 10^{11} M_{\odot}$, $M_{\star} = (3.2^{+0.4}_{-1.1}) \times 10^{11} M_{\odot}$, and $M_{\star} = (2.9^{+0.6}_{-1.8}) \times 10^{11} M_{\odot}$ for these four cases. The stellar mass agrees best with the mass of the de Vaucouleurs component obtained from lensing if we assume a Salpeter IMF. In principle, the mass to light ratios also depend on the age of the galaxy and its metallicity. According to De Lucia et al. (2006), solar metallicity and a formation redshift of 3 to 5 as used in Grillo et al. (2009) are good assumptions for a galaxy of the measured stellar mass. Thus, the IMF must not be Chabrier or Kroupa like unless a fraction of the de Vaucouleurs component is not of stellar origin, i.e. part of the dark matter follows the light distribution. We measure a mass to light ratio for the stellar component of $\frac{M_{\text{deV}}}{L_B} = (5.3^{+0.8}_{-1.1}) \frac{M_{\odot}}{L_{\odot,B}}$ using gravitational lensing and assuming a NFW-like dark matter halo. If we allow for a group halo at galaxy I, we obtain $\frac{M_{\text{deV}}}{L_B} = (6.2^{+0.8}_{-1.0}) \frac{M_{\odot}}{L_{\odot,B}}$. These results again favor a Salpeter IMF, and are in agreement with the Fundamental Plane results $\frac{M}{L_B} = (4.8 \pm 1.4) \frac{M_{\odot}}{L_{\odot,B}}$ for this galaxy from Grillo et al. (2009). These results hold as long as the metallicity is approximately solar. We compare the mass to light ratio, passively evolved to $z=0$, to Coma galaxies analysed in Thomas et al. (2011). We confirm their trend towards a Salpeter IMF, again disfavouring a Kroupa-IMF. This trend also is seen in Cappellari et al. (2012) for the most massive galaxies. Their data indicate a more Salpeter-like IMF for high velocity dispersion galaxies. The dark to total mass fraction of SDSSJ 1430+4105 rises from the centre outwards,

giving a value of $\frac{M_{\text{dark}}}{M_{\text{tot}}} = (0.4_{-0.10}^{+0.14})$ at the Einstein radius. In this galaxy, we need a significant amount of dark matter in its projected centre to explain the observations.

IV) We compare the 3d densities of total, dark and luminous dark matter with Coma galaxies analysed by Thomas et al. (2007), based on dynamical modelling, especially their Figure 5. Our galaxy has an effective radius of 10.96kpc and a velocity dispersion of $322 \pm 32 \text{ km s}^{-1}$. Concerning the effective radius it is most similar to the Coma galaxies GMP 0144, GMP 4928 and GMP 2921, a cD galaxy, which have effective radii of 8.94 kpc, 14.31 kpc and 16.43 kpc (Thomas et al. 2007) and effective velocity dispersions of $211.8 \pm 0.4 \text{ km s}^{-1}$ and $314.8 \pm 2.9 \text{ km s}^{-1}$ and $\approx 400 \text{ km s}^{-1}$ (Thomas et al. 2007, Corsini et al. 2008). Since our 3 dimensional matter densities are reliably known only between 3 kpc and about 6.5 kpc we decide to compare the matter densities at 3 kpc. At this radius the matter density values of Thomas et al. (2007) are reliable as well. At the same time this radius is within the core radius (r_c in Table 2 of Thomas et al. 2007) for all 3 GMP galaxies and thus the densities at this radius define the central dark matter densities in these galaxies. We read off dark matter and total densities of $6 \times 10^{-2} M_{\odot} \text{ pc}^{-3}$ and $3 \times 10^{-1} M_{\odot} \text{ pc}^{-3}$ for GMP 0144, of $1.5 \times 10^{-2} M_{\odot} \text{ pc}^{-3}$ and $2 \times 10^{-1} M_{\odot} \text{ pc}^{-3}$ for GMP 4928 and $1 \times 10^{-1} M_{\odot} \text{ pc}^{-3}$ and $3 \times 10^{-1} M_{\odot} \text{ pc}^{-3}$ for GMP 2921. For SDSSJ 1430+4105 these numbers are $4 \times 10^{-2} M_{\odot} \text{ pc}^{-3}$ and $3.5 \times 10^{-1} M_{\odot} \text{ pc}^{-3}$ for the dark matter and the total density at 3 kpc with fractional errors of about 25%. This means that the dark matter and total densities at 3 kpc for our galaxy and the 3 Coma galaxies are comparable, and that the ratio of dark to total matter density of about 1:10 is consistent within the error with the ratios of 1:5 and 1:13 for the non-central Coma galaxies.

Acknowledgements We acknowledge the support of the European DUEL Research Training Network, Transregional Collaborative Research Centre TRR 33, and Cluster of Excellence for Fundamental Physics, further the use of data from the Sloan Digital Sky Survey, and the Hubble Space Telescope. Further we are grateful to the SLACS collaboration for discovery and follow up observations of the galaxy scale lens sample SDSSJ 1430+4105 is part of. Based on observations made with the NASA/ESA Hubble Space Telescope, obtained from the data archive at the Space Telescope Institute. STScI is operated by the association of Universities for Research in Astronomy, Inc. under the NASA contract NAS 5-26555. We thank Natascha Greisel for making SFH fits for us and Niv Drory for providing us with his SFH-fit code SEDfits. We thank Claudio Grillo for many discussions and comments on this topic. We thank Jens Thomas for discussions about dynamical constraints on Coma galaxies. We thank Ralf Bender for discussions. We want to thank the anonymous referee for the numerous and elaborate comments, helping to improve the manuscript and making it more concise and understandable.

REFERENCES

Abazajian, K., et al., 2009, ApJS, 182, 543
Adelman-McCarthy, J.K., et al., 2007, ApJS 172, 634

Auger, M. W., Treu T., Bolton A. S., Gavazzi R., Koopmans L. V. E., Marshall P. J., Bundy K., Moustakas L. A., 2009, ApJ, 705, 1099
Auger, M. W., Treu T., Bolton A. S., Gavazzi R., Koopmans L. V. E., Marshall P. J., Moustakas L. A., Burles S., 2010, ApJ, 724, 511
Barkana, R., 1998, ApJ, 502, 531
Barnabè, M., Czoske, O., Koopmans, L. V. E., Treu, T., Bolton, A. S., and Gavazzi, R., 2009, MNRAS, 399, 21
Barnabè, M., Auger, M. W., Treu, T., Koopmans, L. V. E., Bolton, A. S., Czoske, O., Gavazzi, R. 2010, MNRAS, 406, 2339
Bell, E. F. McInthosh, D. H., Katz, N., Weinberg, M. D. 2003 ApJ, 585, 117
Bertin, G., Liseikina, T., & Pegoraro, F., 2003, A&A, 405, 73
Blumenthal, G. R., Faber, S. M., Flores, R., and Primack, J. R., 1986, ApJ, 301, 27
Bolton, A. S., Burles, S., Schlegel, D. J., Eisenstein, D. J., Brinkmann, J., 2004, ApJ 127, 1860
Bolton, A. S., Burles, S., Koopmans, L. V. E., Treu, T., Moustakas, L. A., 2006, ApJ, 638, 703
Bolton, A. S., Burles, S., Koopmans, L. V. E., Treu, T., Gavazzi, R., Moustakas, L. A., Wayth, R., Schlegel, D. J., 2008, ApJ, 682, 964
Bolton, A. S., Treu, T., Koopmans L. V. E., Gavazzi R., Moustakas L. A., Burles S., Schlegel D. J., and Wayth R., 2008, ApJ, 684, 248
Bruzual, G., & Charlot, S., 2003, MNRAS, 344, 1000
Bullock, J. S., Kolatt, T. S., Sigad, Y., Somerville, R. S., Kravtsov, A. V., Klypin, A. A., Primack, J. R., and Dekel, A., 2001, MNRAS, 321, 559
Cappellari, M., et al., 2006, MNRAS, 366, 1126
Cappellari, M., et al., arXiv:1202.3308
Chabrier, G., 2003, PASP, 115, 809
Cohn, J. D., Kochanek, C. D., McLeod, B. A., Keeton, C. R., 2001, ApJ, 554, 1216
Corsini, E. M., Wegner, G., Saglia, R. P., Thomas, J., Bender, R., Thomas, D., 2008, ApJS, 175, 462
De Lucia, G., Springel, V., White, S. D. M., Croton, D., Kauffmann, G., 2006, MNRAS, 366, 499
Drory, N., Feulner, G., Bender, R., Botzler, C. S., Hopp, U., Maraston, C., Mendes de Oliveira, C., Snigula, J., 2001, MNRAS, 325, 550
Drory, N., Feulner, G., Hopp, U., Maraston, C., Snigula, J., Hill, G. J., 2004, ApJ, 608, 742
Duffy, A. R., Schaye, J., Kay, S. T., Dalla Vecchia, C., Battye, R. A., Booth, C. M., 2010, MNRAS, 405, 2161
El-Zant, A., Shlosman, I., & Hoffman, Y. 2001, ApJ, 560, 636
Faber, S. M., Jackson, R. E., 1976, ApJ 204, 668
Fadely, R., Keeton, C. R., Nakajima, R., and Bernstein, G. M. 2010, ApJ, 711, 246
Fukugita, M., Hoogan, C. J., Peebles, P. J. E., 1998, ApJ, 503, 518
Gavazzi, R., Treu, T., Koopmans, L. V. E., Bolton, A. S., Moustakas, L. A., Burles, S., Marshall, P. J., 2008, ApJ, 677, 1046
Gelman, A., Carlin, J. B., Stern, H.S., Rubin, D. B. 1995, Bayesian Data Analysis, New York: Chapman & Hal/CRC
Gerhard, O., Kronawitter, A., Saglia, R. P., Bender, R.,

2001, AJ, 121, 1936
 Gnedin, O. Y., Kravtsov, A. V., Klypin, A. A., Nagai, D., 2004, ApJ 616, 16
 Grillo, C., Lombardi, M., & Bertin, G., 2008, A&A, 477, 397
 Grillo, C., et al., 2008, A&A, 486, 45
 Grillo, C., Gobat, R., Lombardi, M., Rosati, P., 2009, A&A, 501, 461
 Grillo, C., Eichner, T., Seitz, S., Bender, R., Lombardi, M., Gobat, R., Bauer, A., 2010, ApJ, 710, 372
 Jesseit, R., Naab, T., & Burkert, A., 2002, ApJ, 571, 89
 Johnston, D. E., et al., 2007, arXiv:0709.1159
 Keeton, C. R., 2001, ApJ, 561, 46
 Keeton, C. R., 2001, Preprint (astro-ph/0102340)
 Koester, B. P., et al., 2007, ApJ, 660, 239-255
 Koopmans, et al., 2006, ApJ, 649, 599
 Koopmans, L. V. E., et al., 2009, ApJ 703, L51
 Kroupa, P., 2001, MNRAS, 322, 231
 Lagatutta, D. J., et al., 2010, ApJ, 716, 1579
 Ma, C.-P. & Boylan-Kolchin, M. 2004, PhRvL, 93, 1301
 Maraston, C., 2005, MNRAS, 362, 799
 Navarro, J. F., Frenk, C. S., White, S. D. M. ApJ, 1996, 462, 563
 Oyaizu, H., Lima, M., Cunha, C. E., Lin, H., Frieman, J., Sheldon, E. S., 2008, ApJ 674, 768
 Peng, C. Y., Ho, L. C., Impey, C. D., & Rix H. W., 2002, AJ, 124, 266
 Pu, S. B., Saglia, R. P., Fabricius, M. H., Thomas, J., Han, Z., 2010, A % A, 516, A4
 Rozo, E., et al., 2009, ApJ, 699, 768-781
 Saglia, R. P., Bertin, G., & Stiavelli, M., 1992, ApJ, 384, 433
 Salpeter, E. E., 1955, ApJ, 121, 161
 Sanderson, A. J. R., Ponman, T. J., Finoguenov, A., Lloyd-Davis, E. J., Markevitch, M., 2003, MNRAS, 340, 989
 Sèrsic, J. L., 1963, Boletín de la Asociación Argentina de Astronomía La Plata Argentina, 6, 41
 Song, J., Mohr, J. J., Barkhouse, W. A., Warren, M. S., Rude, C., 2012, ApJ, 747, 58
 Suyu, S. H., Marshall P. J., Blandford R. D., Fassnacht C. D., Koopmans L. V. E., McKean J. P., Treu T., 2009, ApJ, 691, 277
 Suyu, S. H., Marshall P. J., Auger M. W., Hilbert S., Blandford R. D., Koopmans L. V. E., Fassnacht C. D., Treu T., 2010, ApJ, 711, 201
 Thomas, J., Saglia, R. P., Bender, R., Thomas, D., Gebhardt, K., Magorrian, J., Corsini, E. M., and Wegner, G., 2007, MNRAS, 382, 657
 Thomas, J., Saglia, R. P., Bender, R., Thomas, D., Gebhardt, K., Magorrian, J., Corsini, E. M., and Wegner, G., 2009, ApJ, 691, 770
 Thomas, J., Saglia, R. P., Bender, R., Thomas, D., Gebhardt, K., Magorrian, J., Corsini, E. M., Wegner, G. and Seitz, S., 2011, MNRAS, 415, 1, 545
 de Vaucouleurs, G., 1948, Annales d'Astrophysique, 11, 247
 Wayth, R. B., Webster, R. L., 2006, MNRAS, 372, 3, 1187
 Weijmans, A.-M., Krajnović, van de Ven G., Oosterloo T. A., Morganti R., de Zeeuw P. T., 2008, MNRAS, 383, 1343
 Wright, C. O., Brainerd, T. G., 2000, ApJ, 534, 34
 Young, L. M., et al., 2011, MNRAS, 414, 940
 Xanthopoulos, E. et al., 1998, MNRAS, 300, 649

APPENDIX A: ADDITIONAL STRONG LENSING MODELS

To check for the robustness of the previously derived lensing results, we also examine some different strong lensing models to the ones presented in Secs. 3.1 and 3.2. These models confirm the previous results without adding new implications for the results, therefore we add these models in this appendix.

Model Ia : To account for the environment, we include the galaxy group explicitly as a SIS profile centred at galaxy I in Tab. 3. We use a prior on the group Einstein radius of $b_{\text{group,prior}} = (3.6 \pm 1.5)''$, as derived in Sec. 3.2. The results and 68 % c.l. marginalised errors of this SIE+GI (Model Ia) case are: $b = (1.45_{-0.02}^{+0.02})''$, $q = (0.81_{-0.04}^{+0.04})$, $\Theta_q = (-17.4_{-4.0}^{+3.9})^\circ$ and $b_{\text{group}} = (4.6_{-1.4}^{+1.6})''$, see Fig. A1 for the derived parameter errors. This plot shows an anticorrelation of b and b_{group} . This is expected since the total convergence needed at the position of the main lens can either be provided by the main lens or by the mass associated with GI. We also include the environment as external shear, as calculated in Sec B1, see Model Ib in Appendix A. This has only small effects on the derived parameter values.

Model Ib : Model Ib is for a SIE with external shear γ , hence it has 1 more free parameter relative to Model Ia. The external shear priors are based on the environment models derived in Sec. 2.2 and Appendix B: We use $\gamma_{\text{prior}} = (0.012 \pm 0.031)$ and $\Theta_{\gamma,\text{prior}} = (-10 \pm 25)^\circ$. The marginalised errors are: $b = (1.50_{-0.69}^{+0.80})''$, $q = (0.81_{-0.07}^{+0.08})$, $\Theta_q = (-13.4_{-8.7}^{+12.5})^\circ$, $\gamma = (0.050_{-0.025}^{+0.025})$ and $\Theta_\gamma = (-29.6_{-15.8}^{+7.9})^\circ$. There is a correlation present between the axis ratio q and the external shear γ , reflecting the fact that the shear and the ellipticity can compensate each other in its effects on the deflection angle, since both are pointing in the same direction within $\approx 16^\circ$.

Model IIa : If we add the group GI, we obtain a marginalised steepness value of $\beta = (1.71_{-0.13}^{+0.33})$ together with $b = (2.09_{-0.69}^{+0.80})''$, $q = (0.91_{-0.11}^{+0.05})$, $\Theta_q = (-15.3_{-5.6}^{+10.2})^\circ$ and $b_{\text{group}} = (4.5_{-1.5}^{+1.5})''$. Since there is no correlation between β and b_{group} , the details of the environment implementation have no systematic influence on the derived steepness of the lens mass profile. The shear and convergence provided by the group are $\gamma_{\text{GI}} = \kappa_{\text{GI}} = 0.037$ in agreement with our expectations.

Model IIb : A mass density profile which is flatter than isothermal at the Einstein radius can also be achieved by an isothermal mass distribution with a finite core radius. Therefore, Model IIb is for an isothermal ellipsoid with a core radius (NSIE) with $\beta = 2$ and arbitrary value for the core radius Θ_c . For such a model one expects to also find a demagnified third image, which is not observed. We assume that the demagnified third image in the centre produced by a non-singular mass profile could be detected if its flux exceeds 3σ of the sky+object noise in the image for the brightest source pixel. We exclude a region of $0.2''$ in the centre due to residuals of the galaxy subtraction, where we have no limits on the image fluxes at all. We then get the following marginalised errors: $b = (1.63_{-0.10}^{+0.17})''$, $q = (0.75_{-0.03}^{+0.03})$,

$\Theta_q = (-21.5_{-2.3}^{+2.0})^\circ$ and a core radius of $\Theta_c = (0.11_{-0.075}^{+0.13})''$. However, the best-fitting model is identical to Model I, i.e. purely isothermal. There is a linear dependency between b and Θ_c due to the definition of the non-singular profile: A larger core radius needs to be compensated by a larger lensing strength b to get the same enclosed mass within the Einstein radius.

Model IIIa : In Model IIIa we allow for a dark matter component that is centred on the lensing galaxy. Here, we test if we can improve the modelling by combining the de Vaucouleurs profile with a SIE halo. For the dark matter SIE halo, we impose a prior on the axis ratio based on the Bolton et al. (2008) work of $q_{\text{dark,prior}} = (0.79 \pm 0.12)$. For the errors, we get $b = (1.43_{-0.08}^{+0.05})$, $q_d = (0.71_{-0.02}^{+0.02})$, $\Theta_{q,d} = (-21.9_{-2.6}^{+2.1})^\circ$ and $M_{\text{deV}} = (0.6_{-0.4}^{+0.7}) \times 10^{11} M_\odot$. Since the best-fitting model has a $\chi^2 = 11.8$ and almost zero de Vaucouleurs mass, this implies that a de Vaucouleurs like mass model for the light plus a purely isothermal density profile for the dark matter are not compatible with the data. The Einstein radius of the SIE component and the de Vaucouleurs mass are anticorrelated, forcing the total projected mass within the Einstein radius to be constant.

Model IIIb : Instead of the NFW component, we can also model the dark matter component with a NSIE. We limit the core radius of this component to be between 0 and $50''$, and use the same prior on the axis ratio as before. For the mass of the de Vaucouleurs component, we get: $M_{\text{deV}} = (8.5_{-0.7}^{+1.1}) \times 10^{11} M_\odot$. For the other parameters, we get (see Fig. A2): $q_d = (0.78_{-0.08}^{+0.05})$, $\Theta_q = (-26.0_{-2.4}^{+2.6})^\circ$, $b_d = (19.2_{-10.1}^{+13.0})''$ and $\Theta_c = (24.7_{-12.9}^{+15.5})''$. Again, we note that there is a degeneracy between b_d and Θ_c , emerging from the profile definition. Since there are no observed images for radii larger than $2.32''$, this leaves the upper limit of the core radius Θ_c totally unconstrained. Large Θ_c make this dark matter distribution flat at the Einstein radius, with b_d giving its density value.

Model IVa : We model the mass distribution by a de Vaucouleurs model with the shape parameters following the light profile as stated in Table 1. Therefore, the mass of the de Vaucouleurs component is the only free parameter in this model. The best-fitting light model (Model IVa) in Table A2 has a $\chi^2 = 118$, meaning that a pure de Vaucouleurs profile is a bad fit to the observations. The de Vaucouleurs mass in this case is $M_{\text{deV}} = (15.0_{-0.2}^{+0.2}) \times 10^{11} M_\odot$. This badness of the fit implies that there must be a (dark) mass component not following a de Vaucouleurs profile.

Model Va : Here we do the same as in the Model V before: We combine the 2 component model (Model IIIb) with an explicit description for the galaxy group GI. For the de Vaucouleurs component, we get: $M_{\text{deV}} = (11.5_{-1.5}^{+0.7}) \times 10^{11} M_\odot$. For the other parameters, we get $q_d = 0.74_{-0.10}^{+0.11}$, $\Theta_q = (-21.8_{-5.3}^{+6.7})^\circ$, $b_d = (5.5_{-3.0}^{+4.1})''$, $\Theta_c = (16.4_{-9.1}^{+12.1})''$, and for GI $b_{\text{group}} = (5.1_{-1.6}^{+1.3})''$. As one can see, again there is no significant difference between this model's parameters and the one of Model IIIb. As for the NFW-like dark matter halo, the M_{deV} is increased relative to Model IIIb by introducing the group halo GI.

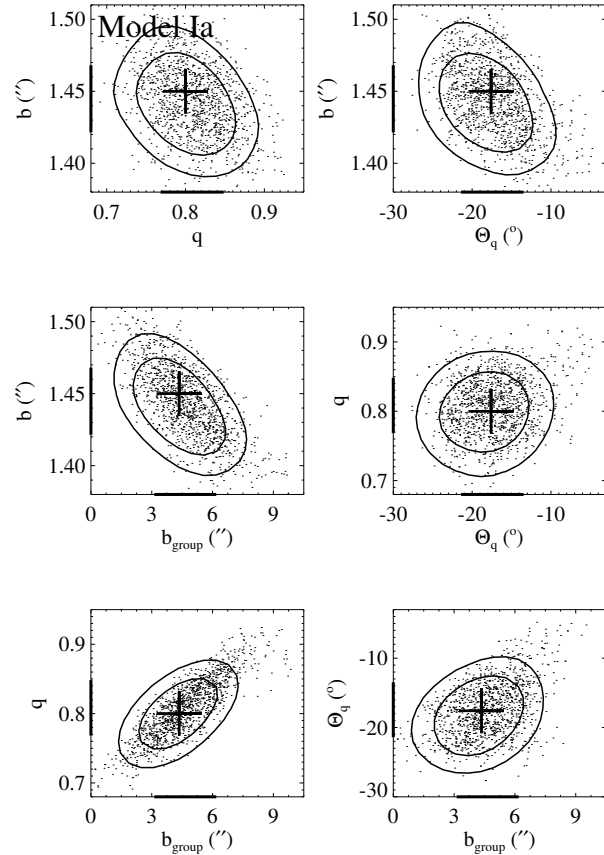


Figure A1. Error estimates of the MCMC for the SIE case with GI (Model Ia), plotted are the individual points of the MCMC together with the 68 and 90 % confidence regions of the distribution. The crosses mark the minimum- χ^2 value from Table 4. The bars on the axes mark the respective 68 % marginalised error intervals.

Model Vb : Model Vb is motivated by the fact that for the preceding models (Models III and V), the axis of the dark matter halo is always offset from that of the light by about -10° , which is statistically significant on a more than 3σ level for Models III and IIIb, see Figs. 7 and A2. At the same time, the axis ratio of the dark matter haloes are consistent with the axis ratio of the stellar component, see Table 1. This could be mimicked by a non accounted external shear which is present if galaxy A is not the centre of the group. From the results for Models Ia, IIa, V and Va, we conclude that if we include the group explicitly as centred on galaxy I the matter gets more aligned with the light. Looking at Model Ib we see that using an external shear instead of GI changes the best-fitting orientation of the total mass distribution more towards the observed light's angle. So, in this Model, we combine Model IIIb with the external shear of Model Ib. In numbers, we get here: $M_{\text{deV}} = (9.9_{-2.7}^{+2.1}) \times 10^{11} M_\odot$, $q_d = (0.77_{-0.10}^{+0.10})$, $\Theta_q = (-14.2_{-11.2}^{+13.0})^\circ$, $c_d = (4.1_{-1.7}^{+4.1})$, $r_{200} = (166_{-55}^{+61})''$, and for the external shear $\gamma = (0.038_{-0.021}^{+0.023})$ and $\Theta_\gamma = (-35.2_{-15.2}^{+9.2})^\circ$. We also note that with this improvement, the dark matter profile becomes more concentrated, at a level expected for galaxies.

Table A1. minimum- χ^2 values and parameter estimates, derived with GRAVLENS for the one component isothermal and powerlaw models

		b (")	q	Θ_q ($^\circ$)	β	Θ_c (")	b_{group} (")	χ^2	d.o.f.	$\frac{\chi^2}{\text{d.o.f}}$
Model Ia	SIE+GI	1.45	0.80	-17.6	2.00 ¹		4.4	8.7	6	1.5
		1.43 – 1.47	0.77 – 0.85	-21.4 – -13.5			3.2 – 6.2			
Model Ib	SIE+es	1.50	0.82	-7.2	2.00 ¹			9.1	5	1.8
		1.48 – 1.52	0.74 – 0.89	-22.1 – -0.9						
Model IIa	PL+GI	2.53	0.93	-13.0	1.60		4.3	7.6	5	1.5
		1.40 – 2.89	0.80 – 0.96	-20.9 – -5.1	1.58 – 2.04		3.0 – 6.0			
Model IIb	NSIE	1.49	0.71	-21.6	2.00 ¹	3.8×10^{-5}		11.5	6	1.9
		1.53 – 1.80	0.72 – 0.78	-23.8 – -19.5		0.035 – 0.24				

¹fixed value

Table A2. minimum- χ^2 values and parameter estimates, derived with GRAVLENS for the two component de Vaucouleurs plus dark matter models

		M ($10^{11}M_\odot$)	q_d	$\Theta_{q,d}$ ($^\circ$)	b_d (")	Θ_c (")	b_{group} (")	χ^2	d.o.f.	$\frac{\chi^2}{\text{d.o.f}}$
Model IVa	deVauc	15.0						118	9	13.1
		14.8 – 15.2								
Model IIIa	deVauc+SIE	0.0004	0.72	-21.5	1.50			11.8	6	2.0
		0.2 – 1.3	0.69 – 0.73	-24.5 – -19.8	1.38 – 1.48					
Model IIIb	deVauc+NSIE	8.2	0.79	-26.9	4.3	4.9		7.6	5	1.5
		7.8 – 9.6	0.70 – 0.83	-28.4 – -23.4	9.1 – 32.2	11.8 – 40.2				
Model Va	deVauc+NSIE+GI	10.0	0.79	-25.5	2.1	3.6	3.6	7.6	4	1.9
		10.0 – 12.2	0.64 – 0.86	-27.1 – -15.1	2.5 – 9.6	7.3 – 28.5	3.5–6.4			

APPENDIX B: ALTERNATIVE DESCRIPTIONS FOR THE LENS ENVIRONMENT

In this Appendix, we discuss 2 alternative scenarios for the environment, firstly a scenario in which the group is only consisting of its members (“clumpy group”) without a reference to a group halo, secondly a scenario where the group is a typical group with 12 members, but centred on galaxy A instead of galaxy I.

B1 Clumpy group

A clumpy group model is obtained if all group mass is considered to be associated to the group galaxies. We describe the galaxies as singular isothermal spheres (SIS) without truncation of their mass profiles and obtain at the position of the lens:

$$\begin{aligned} \kappa_A^{\text{clumpy group}} &= \sum_n \kappa_{\text{SIS},n} \quad , \\ \gamma_A^{\text{clumpy group}} &= \sum_n \gamma_{\text{SIS},n} \quad . \end{aligned} \quad (\text{B1})$$

In this model, the shear and surface density at the location of the lens depends on the 2-dimensional galaxy distribution and not at all on the centre of mass of the group. The galaxies themselves are parametrized only by their positions and velocity dispersions σ_n . The value of the velocity dispersion σ_A for SDSS J1430+4105 is taken from the central velocity dispersion measured by the SDSS. The estimates σ_n for the neighbouring galaxies are obtained from

the Faber-Jackson relation (Faber & Jackson 1976),

$$\sigma_n = \sigma_A \left(\frac{i_n}{i_A} \right)^{0.25} \quad ,$$

where i is the SDSS i band flux of the neighbours and i_A the flux of the lens galaxy A. The shear $\gamma_n(d_n)$ and convergence $\kappa(d_n)$ for a SIS at a projected angular distance d_n from its centre are

$$\kappa(d_n) = \gamma_n(d_n) = \frac{2\pi\sigma_n^2}{c^2 d_n} \left(\frac{D_{\text{ds}}}{D_s} \right) \quad ,$$

with c denoting the speed of light and D_{ds} and D_s mark the angular diameter distances from the lens to the source and from the observer to the source, respectively. The proper (vector) addition of these convergence and shear values yields a prediction of

$$\begin{aligned} \gamma_A^{\text{clumpy group}} &= 0.012 \quad , \\ \kappa_A^{\text{clumpy group}} &= 0.023 \quad . \end{aligned} \quad (\text{B2})$$

The angle of the shear is -10° in the local coordinate system. The fact that we model the galaxies as SISs, ignoring the finite halo sizes which would keep the mass associated to galaxies limited, is not relevant, since finite halo sizes can only lead to lower estimates for the convergence and shear at the position of galaxy A. Therefore, we get an upper limit of the clumpy group estimates using this assumption. As we see in Sec. 3.2, the parameters of the lensing galaxy only mildly depend on the assumptions about the group as long as it is centred on galaxy I. To calculate the mass of this clumpy group, we first need the r_{200} . We adopt the definition of Koester et al. (2007) of r_{200} as a function of number

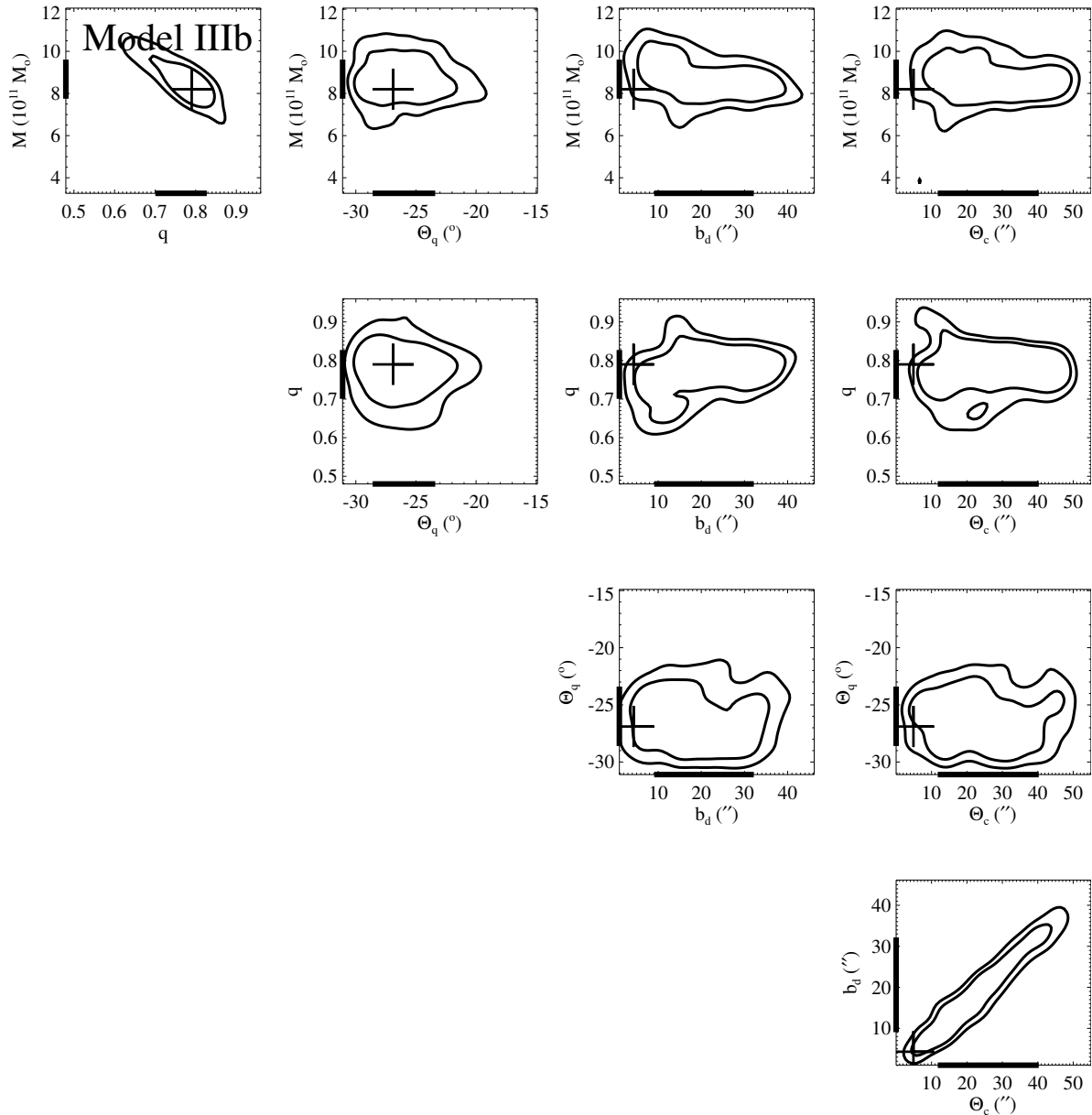


Figure A2. Error estimates of the MCMC for the de Vaucouleurs+NSIE model (Model IIIb), plotted are the individual points of the MCMC together with the 68 and 90 % confidence regions of the distribution. The crosses mark the minimum- χ^2 value from Table 5. The bars on the axes mark the respective 68 % marginalised error intervals. The individual points of the MCMC are omitted for clarity.

of group members. We sum up all mass contributions of member galaxies in Table 3 within this $r_{200} = 3.8'$ centred on A or I, respectively and calculate the total projected mass of the group within its r_{200} : $M_{200} = 5.5 \times 10^{14} M_{\odot}$. This value gives an upper limit of the mass associated with the group, since SIS profiles for its members overestimate the densities of each member at large radii.

B2 Smooth group mass distribution centred at galaxy A

In principle, the assumption of the group being located at A could already be in conflict with the lensing observables. The most secure strong lensing estimate is the observed critical mass $\pi R_{\text{Ein}}^2 \Sigma_{\text{crit}} = 5.43_{-0.16}^{+0.15} \times 10^{11} M_{\odot}$ within the Einstein

radius, obtained from all models in Sec. 4 consistently. We now can model the group – located at A as an NFW or SIS (see Sec. 3.1 for details) profile and estimate its projected mass within the observed Einstein radius. If this halo mass estimate exceeds the observed critical mass, the assumption of this group being a typical group with 12 members and with galaxy A as its centre is already in conflict with the lensing observables.

In Fig. B1 we show the c - r_{200} diagram for a NFW profile. The levels of grey indicate the virial M_{200} mass of a group with parameter values c and r_{200} . The thick solid line marks the transition where the NFW group halo mass within the observed Einstein radius alone (without baryons and dark matter of the galaxy A) exceeds the critical mass, predicting a bigger than the observed Einstein radius. Therefore all

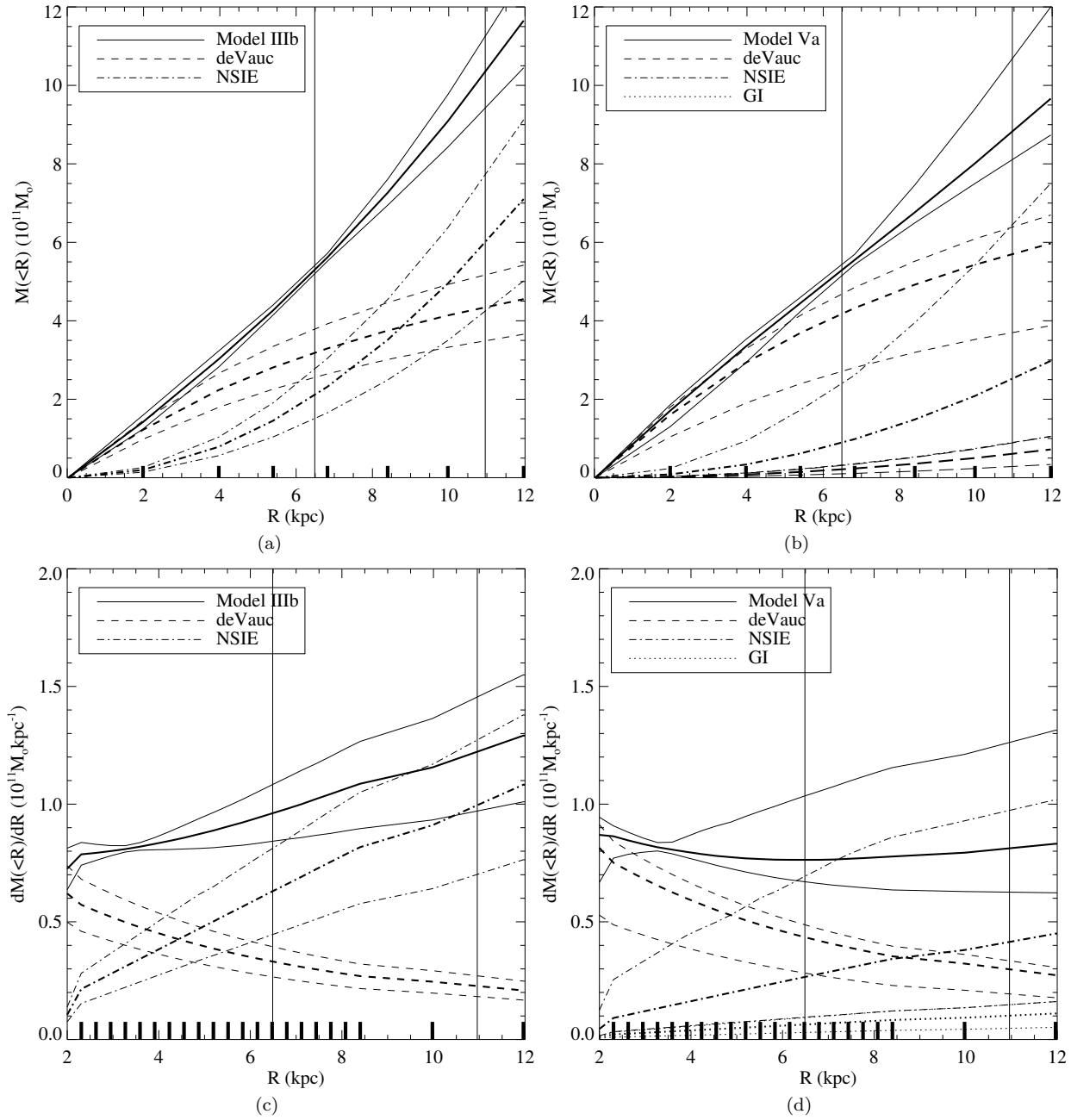


Figure A3. The same as Fig. 13, only for Models IIIb and Va

groups that lie above this line would – from its group halo mass alone – overpredict the observed total projected mass within the Einstein radius and cannot be centred at galaxy A.

In reality, some of the observed mass within the Einstein radius has to be contributed by the stars, giving an even smaller upper limit for the dark matter mass within the Einstein radius. Hence, we plot the analogous curves for the case where the dark matter makes up only a fraction of the total critical mass within the Einstein radius. The dark to total matter fractions shown also in Fig. B1 as dash-dotted lines are $f_{\text{dark}} = 0.55, 0.62, 0.74$. To obtain these numbers, we subtract the stellar mass measurements within the Einstein radius done in Grillo et al. (2009) from the derived

lensing mass within the Einstein radius in this work. If we attribute the missing mass to the group dark matter halo, we get again upper limits for the possible group halo mass contribution within the Einstein radius, allowing us to exclude all groups that would exceed this upper mass limits. Grillo et al. (2009) fit composite stellar population models to the SDSS photometry of this galaxy to derive its stellar mass within the observed Einstein radius. We use the Salpeter IMF stellar masses of Grillo et al. (2009), since these give the highest mass in stars. Now we plot the model group with richness 12 in Fig. B1 to see where it resides. From Johnston et al. (2007), we obtain $c\text{-}r_{200}$ values of 4.22 and 848 kpc for a richness 12 group. Since this group therefore does not fall into the excluded regions of Fig. B1, we cannot exclude A as

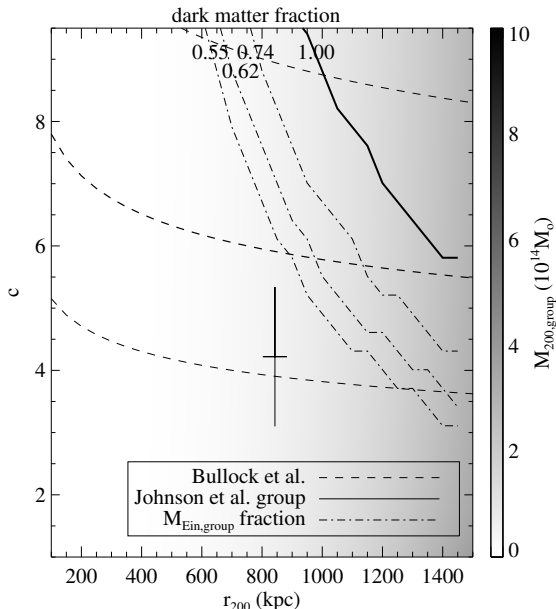


Figure B1. This figure shows the concentration c - r_{200} properties for a NFW halo profile. The levels of grey show the virial masses of the dark matter haloes. Overplotted are several different lines: The dashed lines are the Bullock et al. (2001) c - r_{200} relation with its 1σ error. This marks the area typically populated by galaxy groups. Further we overplot the c - r_{200} values for a typical richness $N=12$ group halo as found by Johnston et al. (2007) with its errorbars. This shows where we expect the group halo to lie approximately in this plane. The dash-dotted lines mark the transition above which more than 55, 62 and 74 % of the observed critical mass within the observed Einstein radius would be made up by the dark matter halo of the group. All group haloes above this dash-dotted line in this c - r_{200} plane overpredict the observed total mass within the Einstein radius, therefore this lines mark regions with excluded group haloes. Since the typical Johnston et al. (2007) group halo lies below this lines, the observed critical mass within the Einstein radius does not exclude A as the group centre. The thick, solid 1.00 line marks the transition where the dark matter group halo alone would provide the observed critical mass within the Einstein radius. Hence along this line no baryons (or dark matter) in the lensing galaxy A would be required at all.

the group centre from the lensing observables. This conclusion also holds in the picture where the group is modelled as SIS. If the group follows a SIS matter profile it has an Einstein radius of $\Theta_E = 3.6 \pm 1.5''$, see Sec. 3.2. This is consistent within the errors with the value derived from the strong lensing models in Sec. 4. Therefore a typical group with richness 12, as seen in the vicinity of SDSSJ 1430+4105, does not violate the observed critical mass within the Einstein radius, nor the Einstein radius itself. Hence, galaxy A could also be the group centre without violating the lensing observables for a typical group of this richness.